

2019-01-01

Electronic Tuning of Dimolybdenum Complexes Through Symmetry Manipulation of Formamidinate Ligands in Their Second Coordination Sphere

Iván Alonso Cervantes Cervantes Martínez
University of Texas at El Paso

Follow this and additional works at: https://digitalcommons.utep.edu/open_etd

 Part of the [Chemistry Commons](#)

Recommended Citation

Cervantes Martínez, Iván Alonso Cervantes, "Electronic Tuning of Dimolybdenum Complexes Through Symmetry Manipulation of Formamidinate Ligands in Their Second Coordination Sphere" (2019). *Open Access Theses & Dissertations*. 2839.

https://digitalcommons.utep.edu/open_etd/2839

This is brought to you for free and open access by ScholarWorks@UTEP. It has been accepted for inclusion in Open Access Theses & Dissertations by an authorized administrator of ScholarWorks@UTEP. For more information, please contact lweber@utep.edu.

ELECTRONIC TUNING OF DIMOLYBDENUM COMPLEXES THROUGH SYMMETRY
MANIPULATION OF FORMAMIDINATE LIGANDS IN THEIR SECOND
COORDINATION SPHERE

IVÁN ALONSO CERVANTES MARTÍNEZ

Master's Program in Chemistry

APPROVED:

Dino Villagrán, Ph.D., Chair

Skye Fortier, Ph.D.

José Bañuelos, Ph.D.

Stephen L. Crites, Jr., Ph.D.
Dean of the Graduate School

Copyright ©

by

Iván Alonso Cervantes Martínez

2019

Dedication

To my family and friends. Gracias por todo.

ELECTRONIC TUNING OF DIMOLYBDENUM SYSTEMS THROUGH SYMMETRY
MANIPULATION OF FORMAMIDINATE LIGANDS IN THEIR SECOND
COORDINATION SPHERE

by

IVÁN ALONSO CERVANTES MARTÍNEZ, B.S.

THESIS

Presented to the Faculty of the Graduate School of
The University of Texas at El Paso
in Partial Fulfillment
of the Requirements
for the Degree of

MASTER OF SCIENCE

Department of Chemistry and Biochemistry
THE UNIVERSITY OF TEXAS AT EL PASO

December 2019

Acknowledgements

I would like to thank my advisor, Dr. Villagrán, for all his support, guidance, patience, knowledge and opportunities he provided me during both my undergraduate and graduate studies. I am forever thankful to him for letting me join his research group since I was a freshman student. He inspired me into the learning about metal-metal bonds and fomented my interest in inorganic and physical chemistry. I would also like to thank my committee members, Dr. Fortier and Dr. Bañuelos, for giving me constructive criticism and for taking the time and attention of giving me advice.

I am grateful for having the chance to work with my present and former lab mates, Nancy, Yulu, Mariana, Sheng, Yanyu, Karen, José, Nathalie, Jacob, Luis, Mario, Roy, Gael, Isabel, Eileen, Mauricio, and Jesus for all the experiences lived together, for letting me discuss with you about chemistry and non-chemistry related topics, as well as for sharing your knowledge, your problems, and your life experiences with me. I must specially thank Nancy for being my mentor while I was as an undergraduate student and for still helping me until nowadays, but mainly for being my friend. I would also like to thank Miguel, Carolina, María, Jesse, Yulu, Luis, Andrew, and Noemi who always offered support and help with research ideas and contributed to my personal growth. Thank you, Marisol, for always being there for me since nine years ago. I would also like to recognize the tremendous effort and dedication of my adopted undergraduate student, Luis Carlos. Thank you for letting me assist you and give you some guidance, as well as for forging a friendship along the way.

I thank my mom, my dad, Néstor, and América for the unconditional support they gave me and for giving me the opportunity to improve myself. I cannot thank enough the sacrifices that they have done for me to be able to reach my goals. I express my gratitude to all the professors

that taught me valuable lessons. Finally, thanks to all my relatives and friends who are there for me in the best and the worst, and who always wish the best for me.

Abstract

Alternative sustainable energy sources are required to decrease our dependence on carbon-based fuels. Small molecule activation is one of the most promising to fulfill global energy demand and maintain a sustainable world. Most of the industrial processes relevant for global energy supply and expenditure involves small molecules and metal catalysts. However, it is still required to gain fundamental insights on how these catalysts achieve such reactions. Dinuclear compounds, namely dimolybdenum complexes, may serve as a good experimental model to understand metal-metal cooperativity and its influence in catalysis.

In Chapter 2, three unsymmetric aryl formamidines were synthesized and characterized through ^1H NMR, LCMS and SC-XRD. Compound **1** was compared with its symmetric analogs through NMR and was synthesized under equivalent conditions of its symmetric isomers. Syntheses of **2** and **3** required a stepwise approach and column but were accomplished, nonetheless. Bond distances in crystal structures manifested that the N=C bond resided on the most electron donating side on the unsymmetric aryl formamidine. and the proton are situated in the unsymmetric aryl formamidines. Furthermore, σ values were obtained for the synthesized ligands (**1** = - 0.075, **2** = - 0.023, **3** = - 0.060).

Chapter 3 discusses synthesis, characterization, and electrochemical studies of dimolybdenum complexes. Crystal structures for **5** and **6** were obtained with metal-metal bond distances of 2.0991 Å and 2.1009 Å, respectively. Cyclic voltammetry (CV) upon **5** depicts a one-electron reversible redox event at - 0.240 V. Electrochemical redox potential of **5** was compared to its symmetric analogs and fell between its homologues. Changing the position of one of the substituents in the phenyl ring tuned the redox behavior of the system. Compounds **6** and **7** display a one-electron reversible redox events - 0.283 V and - 0.260 V, respectively. Redox potentials for

6 and **7** have proximate values between them as well as their average Hammett constant, σ . As σ is constructed to be more negative, the redox potential will decrease for dimolybdenum compounds. Studying unsymmetric aryl formamidine ligands in dimolybdenum complexes gives rise to resourceful tool of electronic tuning empowered by a wide variation of possible substituents for ligand design.

Table of Contents

Dedication.....	iii
Acknowledgements.....	v
Abstract.....	vii
Table of Contents.....	ix
List of Tables.....	xi
List of Figures.....	xii
List of Illustrations.....	xiii
Chapter 1: Introduction.....	1
Chapter 2: Unsymmetric Formamidinium Ligand Design and Its Utilization in Redox Tuning.....	5
2.1 INTRODUCTION.....	5
2.2 EXPERIMENTAL SECTION.....	8
2.2.1 Materials and Methods.....	8
2.2.2 Physical Measurements.....	8
2.2.3 Syntheses.....	8
2.2.3.1 Synthesis of <i>N</i> -3-methoxyphenyl, <i>N'</i> -4-methoxyphenyl-formamidinium ($D^{m,p}AniF$) (1).....	8
2.2.3.2 Synthesis of <i>N</i> -3-methoxyphenyl, <i>N'</i> -2,6-diisopropylphenyl-formamidinium ($Dipp^mAF$) (2).....	9
2.2.3.3 Synthesis of <i>N</i> -2,6-diisopropylphenyl, <i>N'</i> -4-chloro-formamidinium ($ClDippF$) (3).....	9
2.2.3.4 Synthesis of <i>N</i> -2,6-diisopropylphenyl, <i>N'</i> -2,4,6-trimethylphenyl-formamidinium ($MesDippF$) (4).....	10
2.3 X-RAY CRYSTALLOGRAPHY.....	10
2.3.1 $D^{m,p}AniF$	10
2.3.2 $Dipp^mAF$	12
2.3.3 $ClDippF$	14
2.4 RESULTS AND DISCUSSION.....	15
2.5 CONCLUSION.....	20
Chapter 3: Electronic Tuning of Dimolybdenum Complexes by Modification of Ligand Periphery.....	21
3.1 INTRODUCTION.....	21
3.2 EXPERIMENTAL SECTION.....	25
3.2.1 Materials and Methods.....	25

3.2.2 Physical Measurements.....	25
3.2.3 Electrochemical Studies.....	25
3.2.4 Syntheses.....	26
3.2.4.1 Synthesis of Mo ₂ (D ^{m,p} AniF) ₄ (5).....	26
3.2.4.2 Synthesis of Mo ₂ (OAc) ₂ (Dipp ^m AF) ₂ (6).	26
3.2.4.3 Synthesis of Mo ₂ (OAc) ₂ (^p ClDippF) ₂ (7).	27
3.3 X-RAY CRYSTALLOGRAPHY.....	28
3.3.1 Mo ₂ (D ^{m,p} AniF) ₄	28
3.3.2 Mo ₂ (OAc) ₂ (DippAF) ₂	30
3.4 RESULTS AND DISCUSSION.....	32
3.4.1 Syntheses and Structures.....	32
3.4.2 Electrochemistry.....	33
3.5 CONCLUSION	35
Chapter 4: Conclusion.....	38
References	41
Appendix	49
Vita.....	70

List of Tables

Table 2.1. X-ray crystallography data for 1.....	11
Table 2.2. X-ray crystallography data for 2.....	13
Table 2.3. X-ray crystallographic data for 3.	15
Table 2.4. Selected Hammett substituent constants.....	20
Table 3.1. X-ray crystallography data for 5	29
Table 3.2. X-ray crystallography data for 6.....	31
Table 3.3. Selected bond lengths (Å) and bond angles (°) for 5 and 6.	32
Table A.1. Bond lengths (Å) for 1.....	51
Table A.2. Bond angles (°) for 1.....	51
Table A.3. Torsion angles (°) for 1.....	52
Table A.4. Bond lengths (Å) for 2.....	54
Table A.5. Bond angles (°) for 2.....	55
Table A.6. Torsion angles (°) for 2.....	58
Table A.7. Bond lengths (Å) for 3.....	60
Table A.8. Bond angles (°) for 3.....	61
Table A.9. Torsion angles (°) for 3.....	62
Table A.10. Bond lengths (Å) for 5.....	63
Table A.11. Bond angles (°) for 5.....	64
Table A.12. Torsion angles (°) for 5.....	65
Table A.13. Bond lengths (Å) for 6.....	66
Table A.14. Bond angles (°) for 6.....	67
Table A.15. Torsion angles (°) for 6.....	68

List of Figures

Figure 2.1. Crystal structure for 1 with ellipsoids drawn at 50% probability level.....	10
Figure 2.2. Crystal structure for 2 with ellipsoids drawn at 50% probability level.....	12
Figure 2.3. Crystal structures for 3 with ellipsoids drawn at 50% probability level.....	14
Figure 2.4. Stacked ¹ H NMR spectra comparison of HD ^p AniF (green, 1) HD ^{m,p} AniF (blue, 2), and HD ^m AniF (red, 3). See Appendix for single spectra.	17
Figure 3.1. Dependence of E _{1/2} on the Hammett constant for several aryl formamidinato dimolybdenum species.	24
Figure 3.2. Crystal structure for 5 with ellipsoids drawn at 50% probability level.....	28
Figure 3.3. Crystal structure for 6 with ellipsoids drawn at 50% probability level.....	30
Figure 3.4 CV comparison of Mo ₂ (D ^m AniF) ₄ (red, left), Mo ₂ (D ^{m,p} AniF) ₄ (5) (blue, middle), and Mo ₂ (D ^p AniF) ₄ (green, right).....	34
Figure 3.5 Hammett plot of 5 and its symmetric homologues.	34
Figure 3.6. Cyclic voltammogram for 6.	35
Figure 3.7. Cyclic voltammogram for 7.	35
Figure A.1. ¹ H NMR spectrum of D ^p AniF vs CDCl ₃	49
Figure A.2. ¹ H NMR spectrum of D ^m AniF vs CDCl ₃	49
Figure A.3. ¹ H NMR spectrum of 1 vs CDCl ₃	50
Figure A.4 LCMS of 1.	50
Figure A.5. ¹ H NMR spectrum of 2 vs CDCl ₃	53
Figure A.6. LCMS of 2.	53
Figure A.7. ¹ H NMR spectrum of 3 vs CDCl ₃	60
Figure A.8. LCMS of 3.	60
Figure A.9. ¹ H NMR spectrum of 5 vs CDCl ₃	63
Figure A.10. ¹ H NMR spectrum of 6 vs CDCl ₃	66
Figure A.11. ¹ H NMR spectrum of 7 vs CDCl ₃	69

List of Schemes

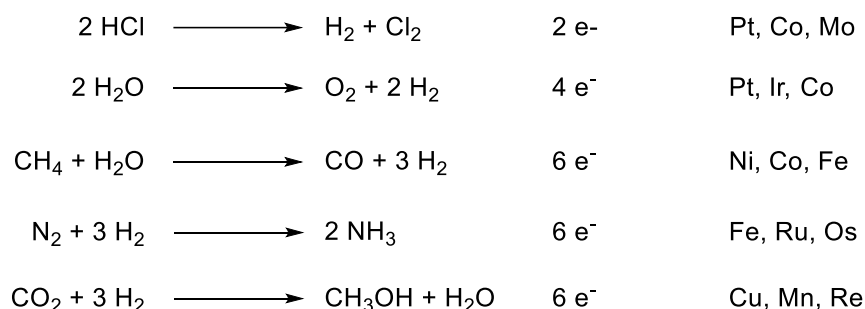
Scheme 1.1. Examples of small molecules requiring multielectron redox chemistry facilitated by transition metals and their compounds. ¹⁸⁻²²	2
Scheme 1.2. Examples of conformations of bimetallic units.	3
Scheme 1.3. Dimolybdenum species with unsymmetric aryl formamidine ligands that may polarize the metal-metal bond.	4
Scheme 2.1. Acid dissociation of benzoic acid and substituted derivatives. Reference reaction for Hammett constants (σ).	5
Scheme 2.2. Proposed unsymmetric formamidines with different electron donating properties on each side (EDG = electron donating groups, EWG = electron withdrawing groups).....	7
Scheme 2.3. Reaction scheme for synthesis of 1.....	15
Scheme 2.4. A. Synthesis of DippFm. B. Reaction scheme for stepwise synthesis of 2 and 3 with DippFm as a precursor.	18
Scheme 2.5. A. Synthesis of MesFm. B. Reaction scheme for stepwise synthesis of 2 and 3 with MesFm as a precursor.	19
Scheme 3.1. Molecular Orbital diagram (d-orbitals) of a quadruply bonded compound.	21
Scheme 3.2. Examples of bidentate (κ^2) ligands that support metal-metal bonds.	23
Scheme 3.3. Possible structural isomers from having unsymmetric ligands.	25
Scheme 3.4. Molecular Orbital diagram (d-orbitals) of a quintuply bonded compound.	36

Chapter 1: Introduction

The consumed global energy is currently obtained through combustion of fossil fuels, over 80% of said energy comes from coal, oil, and natural gas.¹⁻³ The world energy demand has increased since the industrial revolution with the total energy reaching 13.5 TW in 2001, and it is expected to reach 30 TW in 2050 and 46 TW by the end of the century.⁴ The global energy demand has rapidly increased due to the dramatic population growth and the economic activity via industrialization and globalization. In addition, concerns have arisen from unsustainability and the environmental constraints of fossil fuel utilization.^{5,6} The rising emission of greenhouse gases (GHGs) is mainly attributed to combustion of fossil fuels which has a direct influence in some of the contemporary problems of humanity, namely global warming and climate change.^{7,8} Moreover, major dependence on fossil fuels has caused conflict amongst countries that prevents diplomatic conflict resolutions and alters civil security.⁶ Therefore, in the interest of fulfilling the expanding energy demand and alleviating the environmental impact and safety, significant research has been developed in order to take advantage of alternative sustainable global energy sources.⁹⁻¹⁴

Small molecule activation has great potential to deal with global energy consumption. Hydrogen gas (H_2) is set to be the fuel of the future since its combustion produces water. Hence, it generates carbon-free emissions along with high gravimetric energy density.^{15,16} Additionally, H_2 is used as chemical feedstock to synthesize other important energy related compounds (e.g. methane, ammonia, and liquid hydrocarbons). However, hydrogen gas is currently industrially produced through steam reforming of methane which involves fossil fuels and requires high energy input.¹⁷ Water is emerging as the new alternative source for hydrogen production; its splitting yields H_2 and O_2 gas which translates into a carbon-free hydrogen source. Nonetheless, as a hydrogen source water oxidation confronts several problems. This reaction involves a four-

electron transfer process, it is pH dependent, and has huge thermodynamic and kinetic barriers.¹⁰ Similarly, nitrogen (N₂) reduction to ammonia (NH₃) is a significant reaction in terms of energy. The Haber-Bosch process, which is the conventional industrial process to generate NH₃, consumes ~1% of the global energy.¹⁰ The conversion of nitrogen gas to ammonia involves the transfer of six electrons. The activation of other small molecules such as CO, CO₂, or CH₄ also require multielectron redox chemistry. Moreover, these small molecules (Scheme 1.1) contribute as greenhouse contaminants that need practical and economical methods for atmospheric remediation. For example, the Fischer-Tropsch process has become an efficient method for CO conversion in liquid hydrocarbons with the aid of transition metal heterogeneous catalysts. Suggestively, the metal-metal cooperativity found in these catalysts enables the process.¹²



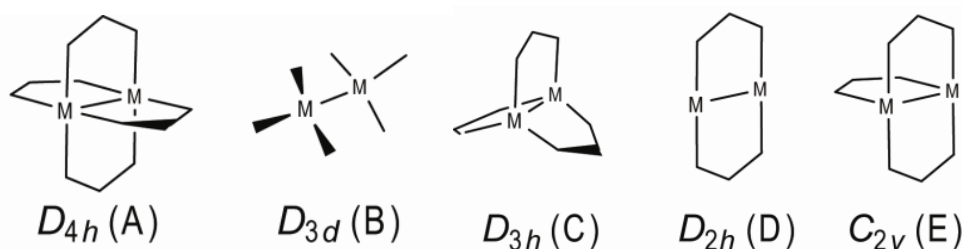
Scheme 1.1. Examples of small molecules requiring multielectron redox chemistry facilitated by transition metals and their compounds.¹⁸⁻²²

Most industrial processes involving catalysts are run at specific operating points which are rarely altered with few exceptions where temperature is gradually increased to compensate deactivation processes. These static conditions are obtained through trial and error until optimal yields and selectivities are found for specific catalysts.²³ However, it is unknown how changing reactions conditions affect a catalyst on a molecular level. In addition, structural changes caused by reaction conditions of the reactant, intermediate, or product influences the catalytic activity.²⁴⁻

²⁷ Although several characterization methods have had significant advances in the study of

heterogeneous catalysts,^{28–30} theoretical descriptions are required in order to better understand the undergoing changes of catalysts. Molecular modeling and simulations have been greatly useful in approaching catalytic function.^{31–33} Nonetheless, experimental models are necessary to validate theories and to further comprehend these systems.

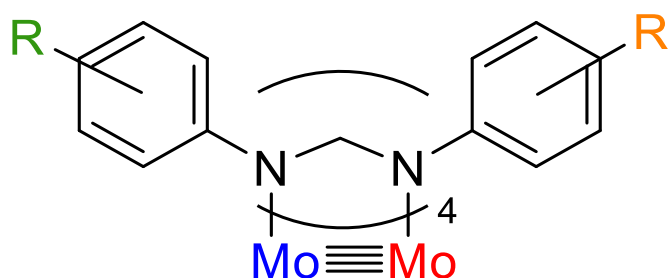
Homogeneous metal complexes can serve as models for heterogeneous catalyst transformations.^{34,35} Their simplicity allows more characterization methods to be available.³⁶ However, mononuclear complexes differ widely from metal surfaces in the sense that the former lack the presence of adjacent metal atoms, which may have a significant influence on the performed chemistry. For instance, β -hydrogen elimination is common in mononuclear late-transition metals,³⁷ whereas analogous clusters yield α -hydrogen elimination.^{38,39} The presence of two metal centers in a complex, especially if they are directly interacting with each other (Scheme 1.2), may depict a better representation of metal-metal cooperativity and how it affects catalytic reactions (e.g. olefin polymerization,⁴⁰ alkyne/methylene coupling reaction,⁴¹ and C-H activation).³⁶



Scheme 1.2. Examples of conformations of bimetallic units.

In this study, bimetallic paddlewheel complexes (Scheme 1.2 A) are utilized as experimental models due to their high d-orbital overlap in order to resemble metal cooperativity in a surface. In the interest of obtaining a high bond order, well-established electrochemical behavior, and a plethora of previously reported species,⁴² dimolybdenum species were the main

subject of study in this project. Formamidines are a great option as ligands since they are bidentate ligands that are reasonably easy to synthesize and characterize, as well as ease of functionalization with a wide variety of functional groups.⁴³ Aryl formamidines and amidines have proved to be useful ligands in pursuance of quintuply bonded species, rendering complexes similar to those depicted in Scheme 1.2 C,D.⁴⁴ Herein, we explored the effect of remote substitution of formamidines in dinuclear metallic systems by applying symmetry descent into our ligand design (Scheme 1.3). Furthermore, the relation of the second coordination sphere to the electronic behavior of dimolybdenum systems was investigated, and the observations will be discussed in a later chapter.



Scheme 1.3. Dimolybdenum species with unsymmetric aryl formamidine ligands that may polarize the metal-metal bond.

Chapter 2: Unsymmetric Formamidine Ligand Design and Its Utilization in Redox Tuning

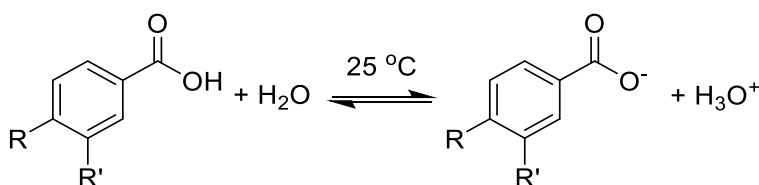
2.1 INTRODUCTION

Ligand design in coordination complexes have served to modulate the electronic properties of metal species as well as to influence the steric environment around the metal coordination sphere. As a result, transition metal and organometallic chemistry, along with homogeneous metal catalysis, have benefited from designing and studying new ligand motifs, e.g pharmaceuticals,⁴⁵ polymers,⁴⁶ catalysts.⁴⁷

Formamidates have been utilized as π -donor ligands for several bimetallic systems because their bidentate nature enables them to bind to different metal atoms in order to build paddlewheel structures.⁴² These ligands have such flexibility in their coordinating abilities that derivatives of these species are designed to connect more than two metals⁴⁸, and they are utilized as precursors for N-heterocyclic carbenes (NHCs).⁴⁹ Moreover, a wide variety of substituents may be added to the amine group in order to manipulate the electronic behavior of the metal with ease of characterization. Functionalization of aryl formamidines has given the opportunity to perform redox tuning in bimetallic complexes by varying the remote substituent.⁵⁰⁻⁵²

$$\log \frac{K}{K_0} = \sigma \rho$$

(Eq. 1)

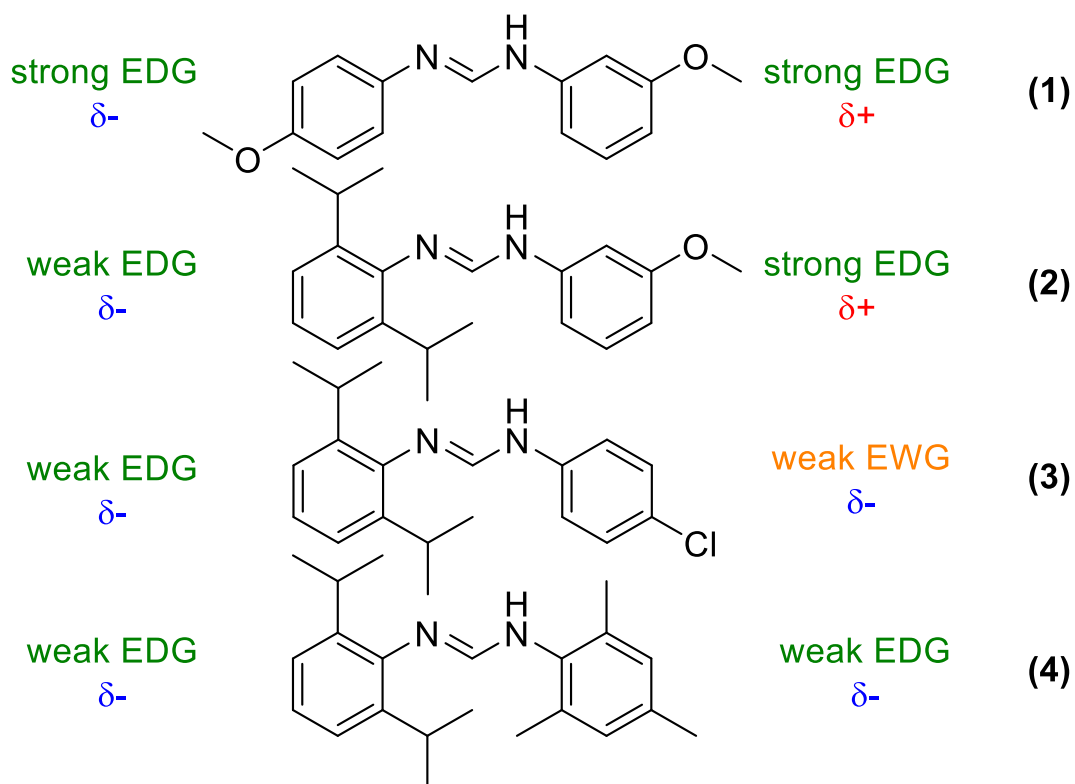


Scheme 2.1. Acid dissociation of benzoic acid and substituted derivatives. Reference reaction for Hammett constants (σ).

Systematic redox tuning with aryl formamidines can be accomplished through inductive and resonance effects exerted by modification of the substituent in their periphery.⁵⁰ Hammett constants (σ) have shown to be a useful tool in measuring the electronic effects of such substituents.⁵³ These constants were first obtained by Louis Hammett in 1937.⁵⁴ He studied the effect of having different substituent groups in the *meta*- and *para*- positions of benzoic acid derivatives, and observed the change in the acid dissociation (K_a) reaction (Scheme 2.1). The Hammett equation (Eq. 1) presents a linear free-energy (ΔG) relationship between equilibrium constants (K/K_0) and reaction rates (ρ) where electron donating groups produce an increase in K_a , and electron withdrawing groups decrease it. This behavior can be transfer into bimetallic complexes redox properties: as the electron donating ability of the substituent increases, the redox potential tends to be more positive (with respect to -H, K_0) which has in addition a direct relation to ΔG .⁵¹ On the other hand, a decrease in redox potential of the bimetallic center occurs when the electron donating abilities of the second coordination sphere decreases due to the presence of electron withdrawing groups. In addition, it has been observed that the position of the substituent in the aromatic ring provides different donating abilities for the ligand.⁵⁵ However, the presence of different functional groups on each side of the formamidine bridging ligand gives rise to new ways of performing electronic tuning in bimetallic complexes.

Herein, it is proposed that aryl formamidines can be synthesized and characterized containing different substituent groups (unsymmetric). The designed formamidines are presented in Scheme 2.2, and they have different substituent groups attributing different electronic strengths and steric effects. Compound **1** was designed with the purpose of observing the effect of varying the position of the functional group in the aryl ring, as well as a proof of principle since its symmetric versions are well reported in literature.⁵⁰ The ligand design for **2-4** includes two bulky

isopropyl groups in *ortho*- positions. Groups with significant steric bulkiness are of interest because they can be potentially used in paddlewheel complexes to obtain systems that present open coordination sites available to perform small molecule activation.⁵⁶ Compounds **2-4** also involve other functional groups with different electron donating properties. These formamidines are intended to be used as ligands provide the foundation for studying diverse environments in dinuclear metallic systems with the possibility of expanding and playing with miscellaneous functional groups and distinct structures.



Scheme 2.2. Proposed unsymmetric formamidines with different electron donating properties on each side (EDG = electron donating groups, EWG = electron withdrawing groups).

2.2 EXPERIMENTAL SECTION

2.2.1 Materials and Methods.

All manipulations were carried under normal atmosphere at room temperature unless otherwise stated. All glassware was oven dried prior to use. The materials used CDCl_3 , acetic acid, *p*-anisidine, triethylorthoformate, and 4-chloroaniline were purchased from Sigma-Aldrich. 2,6-diisopropylaniline was purchased from TCI, while *m*-anisidine was purchased from Oakwood Chemicals both compounds were used as received. DippFm and MesFm were prepared according to literature procedures.¹ The synthetic procedures for the preparation of the proposed aryl formamidines were based from previously reported methods.⁵⁰ HCl , DCM, ethanol, hexanes, ethyl acetate, and diethyl ether were purchased from Fischer Scientific and used as received.

2.2.2 Physical Measurements

All ^1H NMR spectra were recorded on a Bruker 400 MHz NMR spectrometer, and the proton chemical shifts were referenced to CDCl_3 . Mass spectra was obtained using a JEOL AccuTOF JMS-T100LC under ESI+ mode.

2.2.3 Syntheses

2.2.3.1 Synthesis of N-3-methoxyphenyl, N'-4-methoxyphenyl-formamidine ($\text{D}^{\text{m,p}}\text{AniF}$) (1).

Triethyl orthoformate (81.2 mmol), *p*-anisidine (1 mol eq.) and *m*-anisidine (1 mol eq.) were mixed in a 100mL round-bottom flask. The reaction mixture was heated at 140 °C while distilling ethanol until the theoretical amount of ethyl alcohol was collected.¹⁰ Diethyl ether was added to the brown oily product mixture to precipitate a white solid. Sonication helped separate the precipitate from the liquor. The white powder was washed with ether (3 x 30 mL) and hexanes (2 x 30 mL). Yield = 9.334 g, 45%. $R_f = 0.22$. ^1H NMR δ (ppm in CDCl_3): 8.90 (s, 1H, N-H), 8.15 (s, 1H, NCHN-), 7.18 (t, 1H, aromatic C-H), 7.00 (d, 2H, aromatic C-H), 6.86, (d, 2H, aromatic C-H), 6.60 (d, 2H,

aromatic C-H), 6.54 (s, 1H, aromatic C-H), 3.80 (s, 3H, -OCH₃), 3.71 (s, 3H, -OCH₃). ESI-MS (*m/z*): Calcd. 257.12[LH⁺], Found 257.87 [LH⁺].

2.2.3.2 Synthesis of N-3-methoxyphenyl, N'-2,6-diisopropylphenyl-formamidine (Dipp^mAF) (2).

DippFm (0.1025 mol), 1 eq. of *m*-anisidine, and catalytic amounts of HCl (0.05 eq. –approx. 1-2 drops-) were mixed in a 50mL round-bottom flask. The reaction mixture was heated at 140 °C until theoretical amounts of ethanol were collected. A dark orange oil was obtained as a product. Silica column chromatographies were run with ethyl acetate: hexanes (1: 5). Clear crystals were grown from the collected fractions. The crystals were washed with hexanes (3 x 20 mL). Yield = 40%, 12.72 g. R_f = 0.75. ¹H NMR δ (ppm in CDCl₃): 9.98 (s, 1H, N-H), 7.93 (s, 1H, NCHN-), 7.18 (d, 2H, aromatic C-H), 7.14 (t, 1H, aromatic C-H), 7.08 (t, 1H, aromatic C-H), 6.49 (d, 1H, aromatic C-H), 6.43 (d, 1H, aromatic C-H), 6.26 (s, 1H, aromatic C-H), 3.41 (s, 1H, -OCH₃), 3.27 (sept., 2H, C-H), 1.20 (d, 12H, C-H). ESI-MS (*m/z*): Calcd. 311.20 [LH⁺], Found 312.16 [LH⁺].

2.2.3.3 Synthesis of N-2,6-diisopropylphenyl, N'-4-chloro-formamidine (ClDippF) (3).

In a 50mL round bottom flask, DippFm (18.2 mmol) and 1 eq. of 4-chloroaniline were placed along with catalytic amounts of HCl (1 drop). The reaction mixture was heated at 140 °C for 1.5 h while distilling ethanol. The red brown product mixture was with a 5:1 hexanes:ethyl acetate silica chromatography column. Clear crystals were grown through slow evaporation from the corresponding elutions. The crystals were washed with hexanes (3x20mL). Yield: 2.4 g, 42%. R_f = 0.72 ¹H NMR δ (ppm in CDCl₃): 8.75 (s, 1H, N-H), 7.77 (s, 1H, NCHN-), 7.27 (d, 2H, aromatic C-H), 7.18 (t, 1H, aromatic C-H), 6.83 (d, 1H, aromatic C-H), 3.21 (sept., 2H, C-H), 1.20 (d, 12H, C-H). ESI-MS (*m/z*): Calcd. 315.15 [LH⁺], Found 315.20 [LH⁺].

2.2.3.4 Synthesis of *N*-2,6-diisopropylphenyl, *N'*-2,4,6-trimethylphenyl-formamidinium (MesDippF) (4).

In a 10mL round bottom flask, mesityl formimidate (MesFm) and 2,6-diisopropylphenylamine were placed in a 1:1 ratio, along with catalytic amounts of HCl. The reaction was heated at 140 °C until completion of ethanol distillation. The product mixture was diluted in toluene in order to obtain recrystallize the product of interest, but the reaction yielded bismesityl formamidinium.

2.3 X-RAY CRYSTALLOGRAPHY

2.3.1 D^m-PAniF

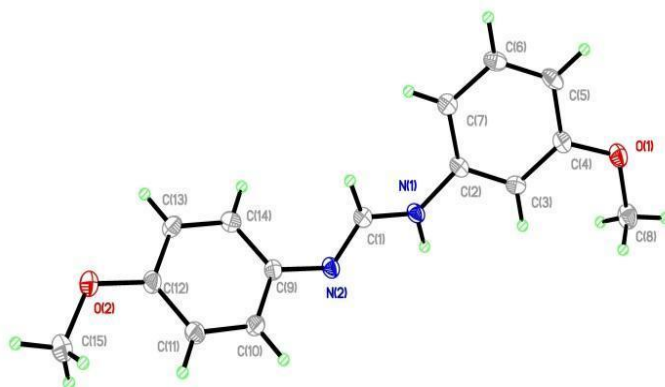


Figure 2.1. Crystal structure for 1 with ellipsoids drawn at 50% probability level.

A specimen of C₂₀HNO₂, approximate dimensions 0.041 mm x 0.082 mm x 0.214 mm, was used for the X-ray crystallography analysis. The X-ray intensity data were measured on a Bruker SMART APEX CCD system equipped with a graphite monochromator and a MoK α fine-focus tube ($\lambda = 0.71073$ Å). The total exposure time was 8 hours. The frames were integrated with the Bruker SAINT software package using a narrow-frame algorithm. The integration of the data using a monoclinic unit cell yielded a total of 14135 reflections to a maximum θ angle of 29.30° (0.73 Å resolution), of which 3455 were independent (average redundancy 4.091, completeness = 99.2%, $R_{\text{int}} = 3.34\%$, $R_{\text{sig}} = 3.48\%$) and 2559 (74.07%) were greater than $2\sigma(F^2)$. The final cell

constants of $a = 7.2915(9) \text{ \AA}$, $b = 5.7809(7) \text{ \AA}$, $c = 30.593(4) \text{ \AA}$, $\beta = 95.398(2)^\circ$, volume = $1283.8(3) \text{ \AA}^3$, are based upon the refinement of the XYZ-centroids of 3052 reflections above $20 \sigma(I)$ with $5.35^\circ < 2\theta < 58.02^\circ$. Data were corrected for absorption effects using the multi-scan method (SADABS). The ratio of minimum to maximum apparent transmission was 0.894. The calculated minimum and maximum transmission coefficients (based on crystal size) are 0.6669 and 0.7459.

The structure was solved and refined using the Bruker SHELXTL Software Package, using the space group $P 1 21/c 1$, with $Z = 4$ for the formula unit, $C_{20}HNO_2$. The final anisotropic full-matrix least-squares refinement on F^2 with 182 variables converged at $R1 = 4.84\%$, for the observed data and $wR2 = 14.68\%$ for all data. The goodness-of-fit was 1.028. The largest peak in the final difference electron density synthesis was $0.433 \text{ e}^-/\text{\AA}^3$ and the largest hole was $-0.241 \text{ e}^-/\text{\AA}^3$ with an RMS deviation of $0.061 \text{ e}^-/\text{\AA}^3$. On the basis of the final model, the calculated density was 1.486 g/cm^3 and $F(000)$, 576 e^- .

Table 2.1. X-ray crystallography data for **1**.

Chemical formula	$C_{15}H_{16}N_2O_2$	
Formula weight	256.30 g/mol	
Temperature	100(2) K	
Wavelength	0.71073 \AA	
Crystal size	0.041 x 0.082 x 0.214 mm	
Crystal system	monoclinic	
Space group	$P 1 21/c 1$	
Unit cell dimensions	$a = 7.2915(9) \text{ \AA}$	$\alpha = 90^\circ$
	$b = 5.7809(7) \text{ \AA}$	$\beta = 95.398(2)^\circ$
	$c = 30.593(4) \text{ \AA}$	$\gamma = 90^\circ$
Volume	$1283.8(3) \text{ \AA}^3$	
Z	4	
Density (calculated)	1.326 g/cm^3	
Absorption coefficient	0.089 mm^{-1}	
$F(000)$	544	

2.3.2 Dipp^mAF

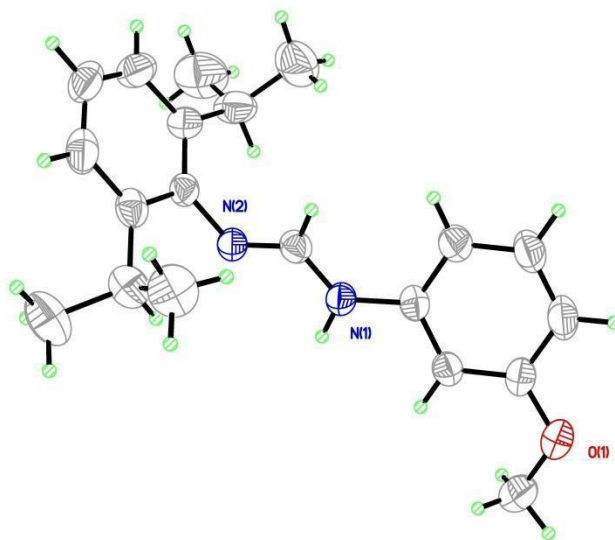


Figure 2.2. Crystal structure for 2 with ellipsoids drawn at 50% probability level.

A specimen of $C_{20}H_{26}N_2O$ was used for the X-ray crystallography analysis. The X-ray intensity data were measured on a Bruker SMART APEX CCD system equipped with a graphite monochromator and a $MoK\alpha$ fine-focus tube ($\lambda = 0.71073 \text{ \AA}$). The total exposure time was 1 hour. The frames were integrated with the Bruker SAINT software package using a narrow-frame algorithm. The integration of the data using an orthorhombic unit cell yielded a total of 25981 reflections to a maximum θ angle of 28.25° (0.75 \AA resolution), of which 9011 were independent (average redundancy 2.883, completeness = 92.2%, $R_{int} = 4.20\%$, $R_{sig} = 4.72\%$) and 4234 (46.99%) were greater than $2\sigma(F^2)$. The final cell constants of $a = 22.979(9) \text{ \AA}$, $b = 23.219(8) \text{ \AA}$, $c = 14.790(6) \text{ \AA}$, volume = 7891.5 \AA^3 , are based upon the refinement of the XYZ-centroids of 3748 reflections above $20 \sigma(I)$ with $4.988^\circ < 2\theta < 42.23^\circ$. Data were corrected for absorption effects using the multi-scan method (SADABS). The ratio of minimum to maximum apparent transmission was 0.915.

The structure was solved and refined using the Bruker SHELXTL Software Package, using the space group $P\ c\ c\ n$, with $Z = 16$ for the formula unit, $C_{20}H_{26}N_2O$. The final anisotropic full-matrix least-squares refinement on F^2 with 431 variables converged at $R1 = 5.89\%$, for the observed data and $wR2 = 21.78\%$ for all data. The goodness-of-fit was 1.029. The largest peak in the final difference electron density synthesis was $0.292\ e^-/\text{\AA}^3$ and the largest hole was $-0.173\ e^-/\text{\AA}^3$ with an RMS deviation of $0.042\ e^-/\text{\AA}^3$. On the basis of the final model, the calculated density was $1.045\ \text{g/cm}^3$ and $F(000)$, 2688 e^- .

Table 2.2. X-ray crystallography data for **2**.

Chemical formula	$C_{20}H_{26}N_2O$	
Formula weight	310.43 g/mol	
Temperature	296(2) K	
Wavelength	0.71073 \AA	
Crystal system	Orthorhombic	
Space group	$P\ c\ c\ n$	
Unit cell dimensions	$a = 22.979(9)\ \text{\AA}$	$\alpha = 90^\circ$
	$b = 23.219(8)\ \text{\AA}$	$\beta = 90^\circ$
	$c = 14.790(6)\ \text{\AA}$	$\gamma = 90^\circ$
Volume	7891.(5) \AA^3	
Z	16	
Density (calculated)	$1.045\ \text{g/cm}^3$	
Absorption coefficient	$0.064\ \text{mm}^{-1}$	
$F(000)$	2688	

2.3.3 CIDippF

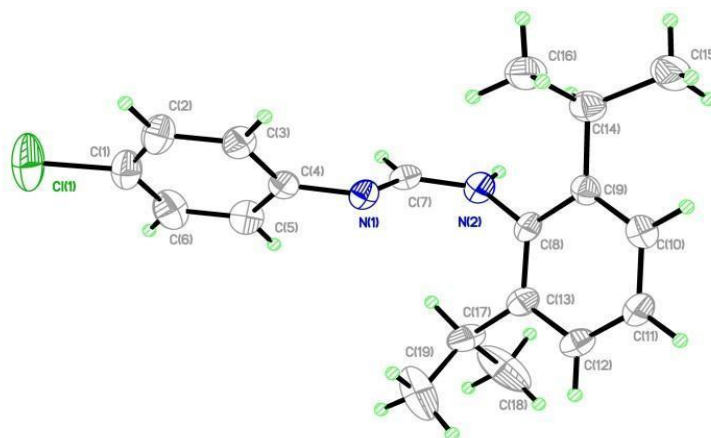


Figure 2.3. Crystal structures for **3** with ellipsoids drawn at 50% probability level.

A specimen of $C_{19}H_{23}ClN_2$ was used for the X-ray crystallography analysis. The X-ray intensity data were measured on a Bruker SMART APEX CCD system equipped with a graphite monochromator and a $MoK\alpha$ fine-focus tube ($\lambda = 0.71073 \text{ \AA}$). The total exposure time was 16 hours. The frames were integrated with the Bruker SAINT software package using a narrow-frame algorithm. The integration of the data using a monoclinic unit cell yielded a total of 13111 reflections to a maximum θ angle of 22.70° (0.92 \AA resolution), of which 2385 were independent (average redundancy 5.497, completeness = 100.0%, $R_{int} = 5.97\%$, $R_{sig} = 4.49\%$) and 1639 (68.72%) were greater than $2\sigma(F^2)$. The final cell constants of $a = 10.4967(15) \text{ \AA}$, $b = 8.6681(8) \text{ \AA}$, $c = 19.6010(18) \text{ \AA}$, $\beta = 97.012(2)^\circ$, volume = $1770.1(3) \text{ \AA}^3$, are based upon the refinement of the XYZ-centroids of 1742 reflections above $20 \sigma(I)$ with $4.655^\circ < 2\theta < 43.86^\circ$. Data were corrected for absorption effects using the multi-scan method (SADABS). The ratio of minimum to maximum apparent transmission was 0.901.

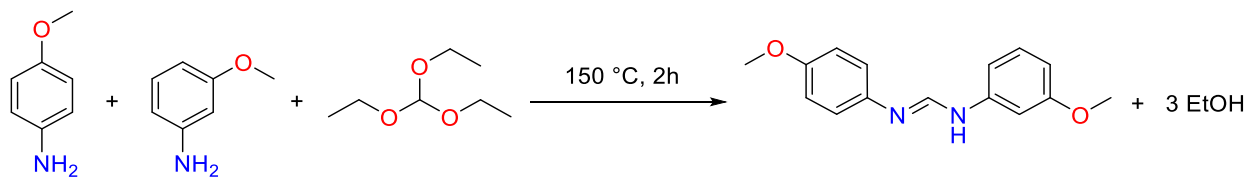
The structure was solved and refined using the Bruker SHELXTL Software Package, using the space group $P 1 21/n 1$, with $Z = 4$ for the formula unit, $C_{19}H_{23}ClN_2$. The final anisotropic full-

matrix least-squares refinement on F^2 with 207 variables converged at $R1 = 4.64\%$, for the observed data and $wR2 = 13.16\%$ for all data. The goodness-of-fit was 1.019. The largest peak in the final difference electron density synthesis was $0.348 \text{ e}^-/\text{\AA}^3$ and the largest hole was $-0.280 \text{ e}^-/\text{\AA}^3$ with an RMS deviation of $0.043 \text{ e}^-/\text{\AA}^3$. On the basis of the final model, the calculated density was 1.181 g/cm^3 and $F(000)$, 672 e^- .

Table 2.3. X-ray crystallographic data for **3**.

Chemical formula	$\text{C}_{19}\text{H}_{23}\text{ClN}_2$	
Formula weight	314.84 g/mol	
Temperature	100(2) K	
Wavelength	0.71073 \AA	
Crystal system	monoclinic	
Space group	$P 1 21/n 1$	
Unit cell dimensions	$a = 10.4967(15) \text{ \AA}$	$\alpha = 90^\circ$
	$b = 8.6681(8) \text{ \AA}$	$\beta = 97.012(2)^\circ$
	$c = 19.6010(18) \text{ \AA}$	$\gamma = 90^\circ$
Volume	$1770.1(3) \text{ \AA}^3$	
Z	4	
Density (calculated)	1.181 g/cm^3	
Absorption coefficient	0.215 mm^{-1}	
$F(000)$	672	

2.4 RESULTS AND DISCUSSION



Scheme 2.3. Reaction scheme for synthesis of **1**.

The synthesis of **1** (Scheme 2.3) was done with the same procedure as its symmetric analogs and as many other symmetric formamidines. The yield agrees with the statistics that of having two unsymmetric molecules per every $D^p\text{AniF}$ and every $D^m\text{AniF}$. Benzene would be used additionally when washing with Et_2O did not remove the residual amounts of the symmetric formamidines.

Benzene would lower the yield but in return we would get a more purified product. **1** is soluble in DCM, Toluene, THF, MeCN, acetone, CHCl₃ and EtOAc. It is not soluble in water, EtOH, MeOH, slightly soluble in diethyl ether, hexanes, and benzene. Presence of the symmetric formamidines was monitored through both TLCs and ¹H NMR. In the case of the TLC, **1** is spotted between its symmetric versions. Similarly, the methine proton is observed in the ¹H NMR at 8.15 ppm, while for D^pAniF there is a downfield shift at 8.24 ppm and D^mAniF has an upfield shift at 8.05 ppm versus the unsymmetric formamidine, see Figure 2.4. Another characteristic comparison of these spectra is the shifts corresponding to —OCH₃. D^pAniF and D^mAniF have a singlet corresponding to six protons at 3.79, and 3.71 ppm, respectively. Differently, **1** presents two singlets integrating three protons each at 3.80 ppm (*para*-) and 3.71 ppm (*meta*-). Crystals for **1** were grown by slow evaporation of Et₂O or acetone. The crystal structure for **1** is depicted in Figure 2.1. The distance for N1-C1 (*meta*- side) is 1.3516 Å and for N2-C1 (*para*- side) is 1.2899 Å. These distances denote the double bond being on the *para*- side of the molecule, where the resonance effect makes a difference for the arrangement of such double bond.

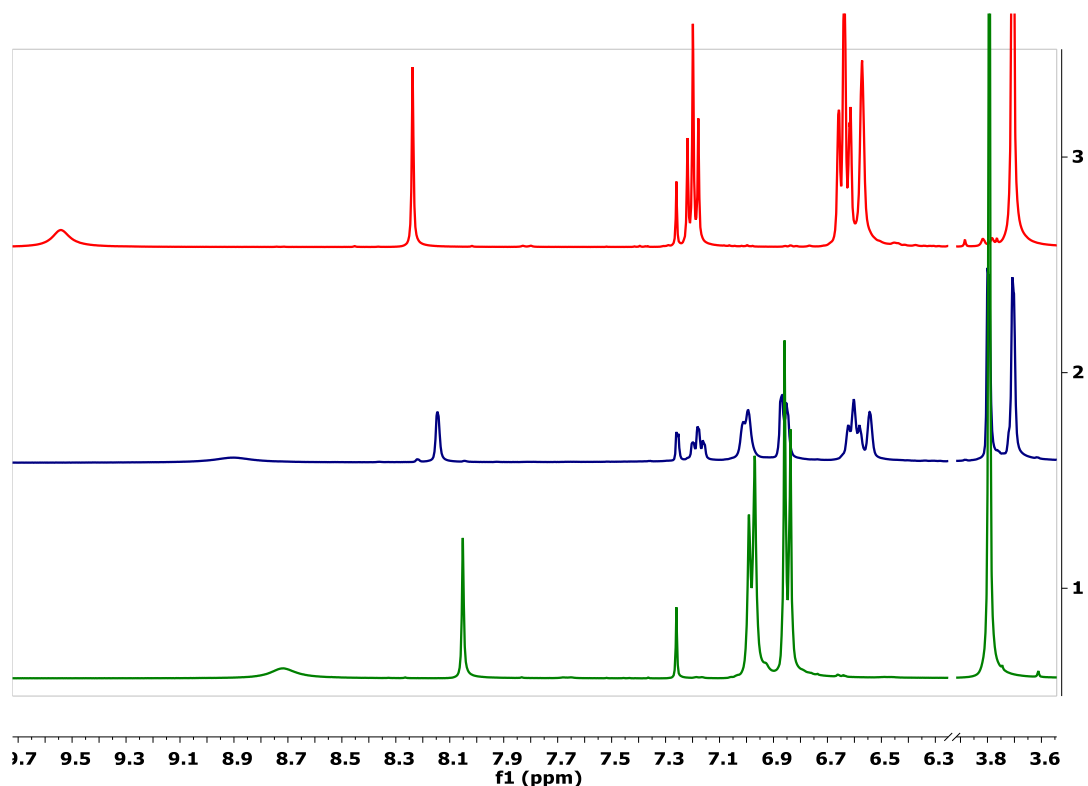
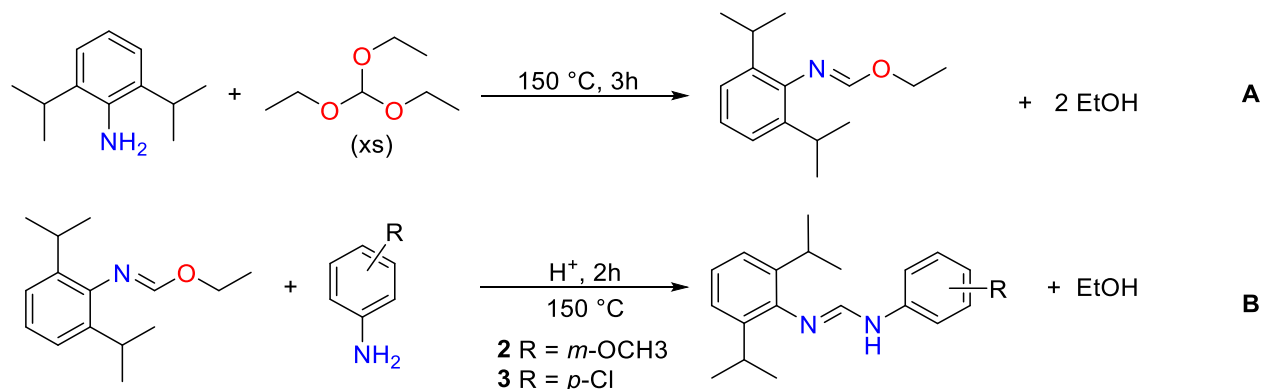


Figure 2.4. Stacked ^1H NMR spectra comparison of HD^pAniF (green, 1) $\text{HD}^{m,p}\text{AniF}$ (blue, 2), and HD^mAniF (red, 3). See Appendix for single spectra.

The synthesis of **2** was attempted in the same manner as for **1**, but D^mAniF was formed instead. DippF was the only product upon the addition of catalytic amounts of acid. Therefore, a stepwise approach with the formation of an intermediate (formimidate) was taken (Scheme 2.4 A). Formimidate synthesis yielded DippFm as the major product, however some DippF was formed as a byproduct. Syringe filters were utilized to isolate the orange oil from the white powder. DippFm over time becomes DippF but the can oil can be recovered by filtration. Reacting DippFm with *m*-anisidine in the presence of one drop HCl yielded **2** (Scheme 2.4 B). The missing percentage is attributed to loss of product during column chromatography. **2** is soluble in DCM, Toluene, THF, MeCN, acetone, benzene, CHCl_3 and EtOAc. It is not soluble in water, EtOH, MeOH. It is slightly soluble in diethyl ether and hexanes. TLC, as with **1**, showed that Dipp^mAF

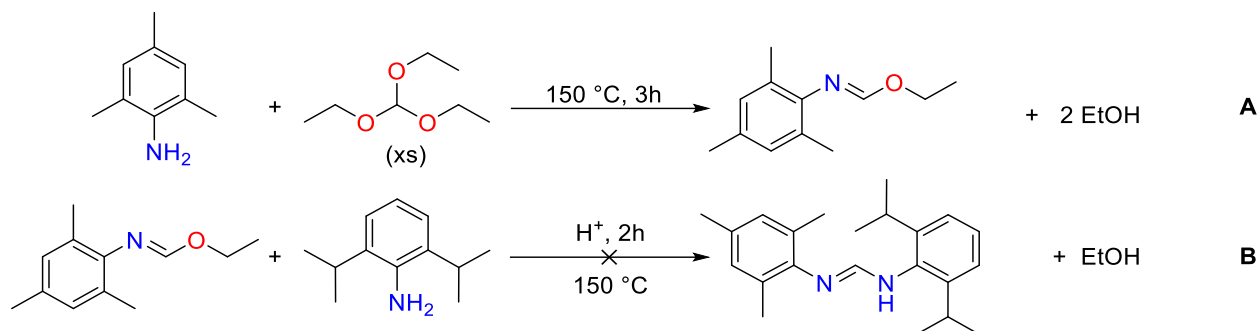
appears between its symmetric analogs. ^1H NMR spectrum suggests the presence of tautomers. Crystals for **2** were grown by slow evaporation from elutions collected from column chromatography. The crystal structure for **2** is depicted in Figure 2.2. Distances for N2-C1 (*iPr*-side), 1.279 Å, and for N1-C1 (*meta*-side), 1.351 Å, corroborate that the double bond sets to the more electron donating side, which corresponds to the half of the diisopropyl groups.



Scheme 2.4. A. Synthesis of DippFm. B. Reaction scheme for stepwise synthesis of **2** and **3** with DippFm as a precursor.

Once the stepwise approach proved to be useful for unsymmetric formamidine formation, **3** was synthesized by using DippFm (Scheme 2.4), as practiced with **2** previously. This reaction yielded 42% of the desired aryl formamidine after purification with silica column chromatography. **3** is soluble in DCM, Toluene, THF, MeCN, acetone, benzene, CHCl₃ and EtOAc. It is not soluble in water, EtOH, MeOH, slightly soluble in diethyl ether and hexanes. TLC trend for unsymmetric ligands remained true since **3** appears between its symmetric variations. ^1H NMR spectra for **3** also suggests the presence of tautomers. There are two septets corresponding to *iPr*- that integrate two protons overall. However, the septet at 3.24 has a significantly higher integration (1.62) than the septet at 3.07. Crystals for **3** were grown by slow evaporation. The crystal structure for **3** is depicted in Figure 2.3. For this ligand, the proton is bound to the diisopropyl side, the nitrogen-

methine distances are 1.292 Å for N2-C7 (*iPr*- side), and 1.338 Å for N1-C7 (*chloro*- side). The N = C bond is favored, as with **1** and **2**, to the more electron donating group.



Scheme 2.5. A. Synthesis of MesFm. B. Reaction scheme for stepwise synthesis of **2** and **3** with MesFm as a precursor.

Different from the other formamidines, **4** was not produced from mixing both anilines, as in with **1**. The stepwise approach for MesDippF only produced the dimesitylformamidine (MesF) when using DippFm and acid in the reaction. The synthetic procedure for **2** and **3** could not be replicated for this formamidine. Therefore, the synthesis of the same formamidine was attempted by using MesFm as the precursor. Although MesFm could be synthesized and isolated in high yields, MesF and DippF (symmetric formamidines) were only produced in the reaction. The similarity in these substituent groups and the proximal Hammett constants suggests that the more different the electron donating properties, the simpler it is to perform synthesis through the stepwise approach.

Table 2.4 displays Hammett constants relevant for the proposed formamidines. Values for substituent that correspond to symmetric formamidines as obtained from literature⁵⁷ and σ for the proposed unsymmetric formamidines were obtained by calculating the average σ values of the all substituents present in the formamidines. Substituents in *ortho*- positions were considered as having the same value as *para*- substituents. For instance, *m*, *p*-OCH₃ (**1**) was measured (-0.268 +

0.115)/2, and -iPr, *m*-OCH₃ (**2**) was calculated ((-0.151*2)+0.115)/3. These values will be useful for next chapter when considering Hammett plots.

Table 2.4. Selected Hammett substituent constants.

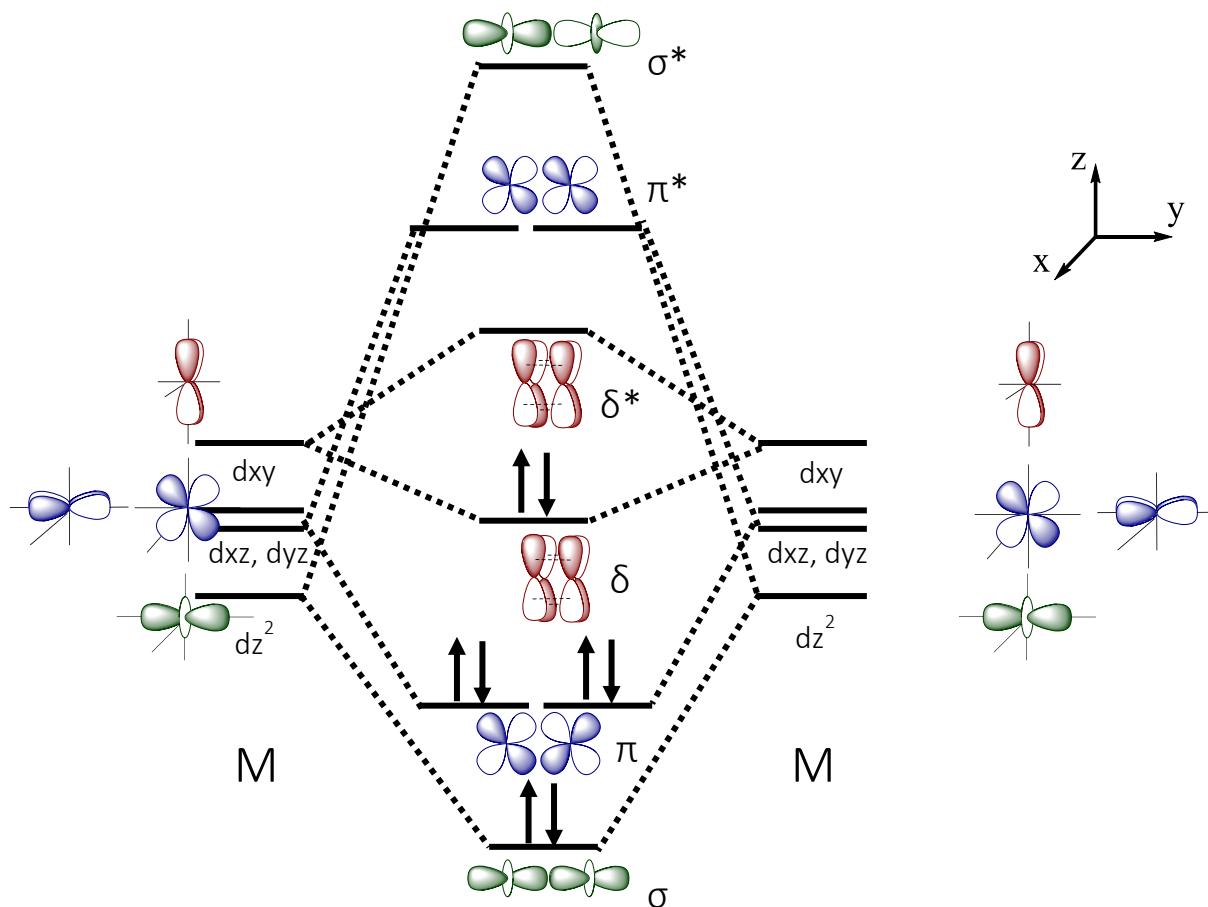
Group	σ
<i>p</i> -OCH ₃	- 0.268
<i>m, p</i> -OCH ₃ (1)	- 0.076
<i>m</i> -OCH ₃	+ 0.115
-iPr, <i>m</i> -OCH ₃ (2)	- 0.062
-iPr	- 0.151
-iPr, <i>p</i> -Cl (3)	- 0.025
<i>p</i> -Cl	+ 0.227
<i>p</i> -CH ₃	- 0.170
-iPr, <i>p</i> -CH ₃ (4)	- 0.162

2.5 CONCLUSION

Formation of **1** can be performed in the same conditions as its symmetric isomers. Nonetheless, production of **2** and **3** required utilizing DippFm as a precursor and column chromatography was necessary to separate unsymmetric products from their symmetric analogs. Crystal structures helped determine where the double bond and the proton are situated in the unsymmetric aryl formamidines. N=C interactions formed where the more electron donating substituent is bound. Differently, synthesis of **4** cannot be achieved through the described methods. Further variations in the experiment need to be explored since facile synthesis of **2** and **3** was achieved without aid of an extravagant catalyst. Complications in formation of **4** is attributed to similar electronic behavior of the involved substituent groups. Larger differences in Hammett constants may contribute to favor formation of unsymmetric aryl formamidines. Lastly, a method was proposed for calculating σ for our ligands.

Chapter 3: Electronic Tuning of Dimolybdenum Complexes by Modification of Ligand Periphery.

3.1 INTRODUCTION

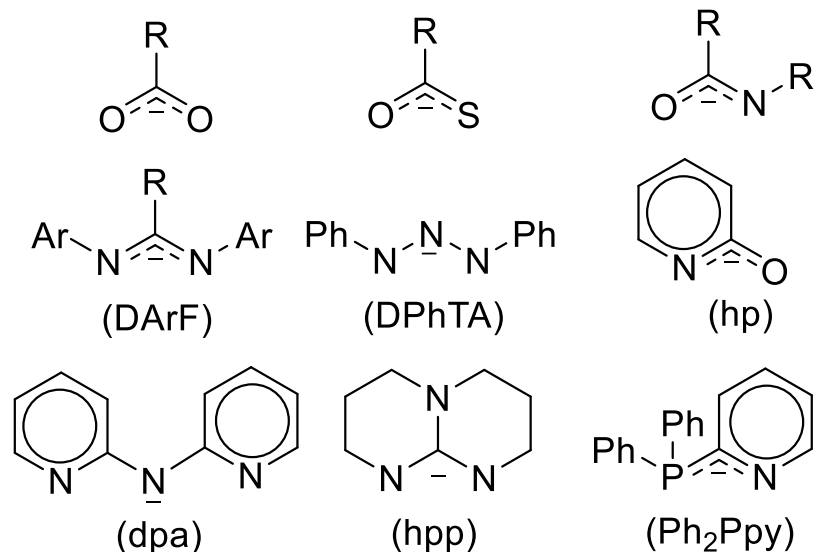


Scheme 3.1. Molecular Orbital diagram (d-orbitals) of a quadruply bonded compound.

Since the discovery of the Re–Re quadruple bond in $\text{Re}_2\text{Cl}_8^{2-}$ 55 years ago, the chemistry of bimetallic complexes with metal-metal bonds has evolved to become an important field of chemistry.⁵⁸ Currently, over a thousand quadruply bonded complexes have been successfully isolated and structurally characterized through single X-ray studies.⁵⁹ This type of paddlewheel complexes has eight metal-based electrons, all of them paired and positioned in one bonding σ

composed of two d_z^2 orbitals, two π bonding interactions, made up of two d_{xy} and d_{yz} and one bonding δ orbital, which is constituted by the overlap between the d_{xy} orbitals giving it a bond order of four (Scheme 3.1). In addition, bimetallic entities such as $M_2^{4+/5+}$ ($M = \text{Cr, Mo, W}$) where an electron is removed have an electronic configuration in which there is certainty as to the shape of the occupied orbital by the unpaired electron, namely a δ interaction. Differently, mononuclear systems often present ambiguity about the type of single-occupied MO (SOMO) because of low local symmetry.³⁶ Hence, dimetal units provide better theoretical and experimental studies with clearer results than mononuclear compounds.

Advances in bimetallic chemistry has been in part due to ligand design. Ligand control over transition metal complexes is plays a major role in homogeneous catalysis^{60,61} and electron transfer reactions.⁶² Substitution of the halide ions by bidentate carboxylate anions brought about an immediate growth in the field. Synthesis and characterization of hundreds of compounds with two metal atoms bridged by four monoanionic species, with paddlewheel or tetragonal structures (commonly recognized as having a D_{4h} symmetry).⁶³ Group six metals (Cr, Mo, W) as well as other metals such as Ru, and Rh are capable of forming such structural types.⁶⁴ Utilization of different types of ligands such as formamidinates and guanidinates (Scheme 3.2) initiated the development of bimetallic complexes with other transition metals, allowing the isolation of the first Ni_2^{5+} complex having a bond order of $1/2$,⁶⁵ as well as the first V_2^{4+} ,⁶⁶ $\text{Fe}_2^{2+,3+}$,^{67,68} $\text{Co}_2^{3+,4+,5+}$,⁶⁹ and $\text{Pt}_2^{4+,5+,6+}$,⁷⁰ compounds.



Scheme 3.2. Examples of bidentate (κ^2) ligands that support metal-metal bonds.

The electronic behavior of bimetallic complexes can be manipulated by varying the nature of the coordinating molecules, by promoting steric effects, and by playing with substituents in the periphery. Nonetheless, changing the first coordination sphere may significantly affect the redox potential of the species. Steric hindrance usually prevents certain interactions to favor others. Altering the second coordination sphere of ancillary ligands on the metal unit modifies the energy of the orbitals, thus modulating redox potentials and photophysical properties of the unit.^{71,72} Redox control over bimetallic entities can potentially be utilized to promote selectivity, and reach desired potentials for different applications. In fact, dinuclear compounds have been successfully used as antitumor agents⁷³, platforms for supramolecular structures⁷⁴, and catalysts.^{75,76} Therefore, the electron transfer process can be influenced through substituent effects on the ancillary ligands with minimum change in the coordination geometry. Tong Ren and his group first showed that redox potentials on Ni_2L_4 and Mo_2L_4 substituted aryl formamidinate complexes can be tuned from variations on the functional groups on the periphery, see Figure 3.1.^{77,78} Later work was performed

with Cr_2L_4 by Eglin.⁷⁹ However, systematic studies of substituent effects on bimetallic centers are scarce and there is more left to know about their electronic properties.

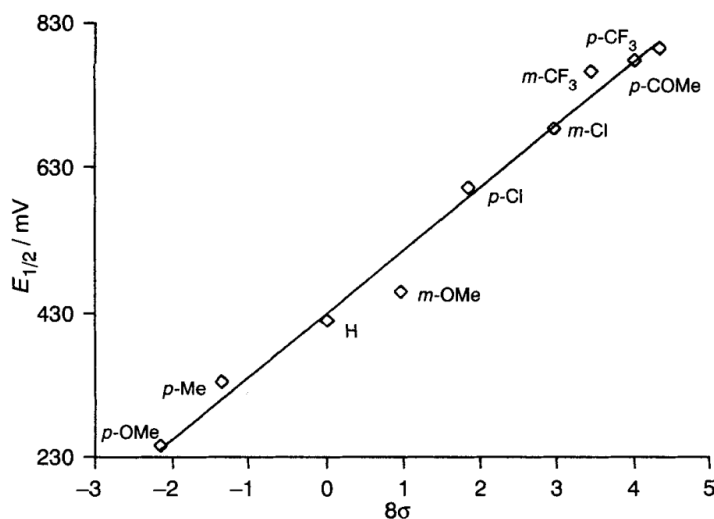
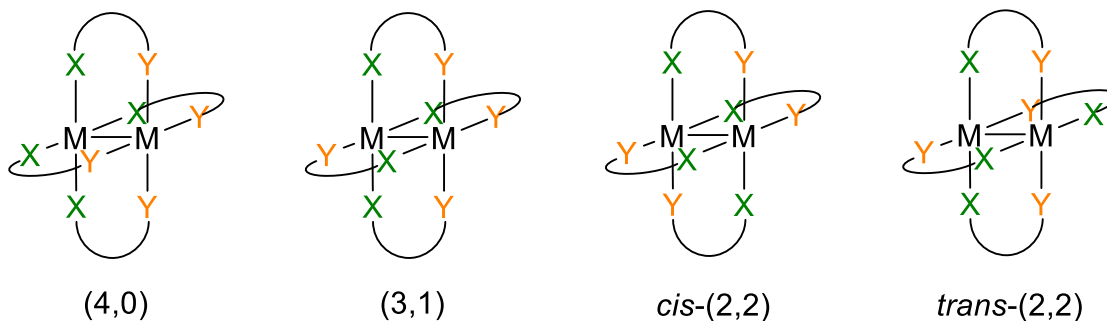


Figure 3.1. Dependence of $E_{1/2}$ on the Hammett constant for several aryl formamidinato dimolybdenum species.⁷⁸

Herein, it is proposed that using unsymmetric formamidinates as ancillary ligands to dimolybdenum species will provide a better understanding and a resourceful tool to tune the electronic properties of bimetallic complexes. Given the possibility of producing structural isomers (Scheme 3.3), it is of our interest to form the (4,0) or (3,1) isomers in order to potentially promote a metal-metal bond polarization. However, isolating these structural isomers has been synthetically challenging for chemists. Berry and his group have reported the only (4,0) isomer for dimolybdenum complexes.^{80,81} Notwithstanding, (2,2) isomers can be studied by observing change in the redox behavior caused by the second coordination sphere. Electrochemical studies were performed in a series of dimolybdenum in order to explore the redox behavior. We were able to probe the electronic tuning capabilities of aryl formamidines in bimetallic compounds with further redox manipulation by asymmetrical ligand synthesis.



Scheme 3.3. Possible structural isomers from having unsymmetric ligands.

3.2 EXPERIMENTAL SECTION

3.2.1 Materials and Methods

All reactions and manipulations were conducted under a nitrogen atmosphere, using either a nitrogen glovebox or standard Schlenk line techniques unless otherwise stated. Solvents used were purified under argon using a Pure Process Technology solvent purification system or degassed under nitrogen. Commercially available chemicals methyllithium (1.6 M MeLi/Et₂O), n-butyllithium (2.5 M BuLi/Hex), sodium methoxide (0.5 M NaOCH₃/MeOH), molybdenum carbonyl, *o*-dichlorobenzene, and acetic anhydride were purchased from Sigma Aldrich and used as received. Mo₂OAc₄,⁸² Mo₂(D^pAniF)₄,⁷⁸ and Mo₂(D^mAniF)₄^{78,83} were synthesized as reported in literature.

3.2.2 Physical Measurements

All ¹H NMR spectra were recorded on a JEOL 600 MHz and a Bruker 400 MHz NMR spectrometers. All proton chemical shifts were referenced to CDCl₃. Mass spectra were obtained using a JEOL AccuTOF JMS-T100LC under ESI+ mode.

3.2.3 Electrochemical Studies

Electrochemical analyses by cyclic voltammetry (CV) and differential pulse voltammetry (DPV) were collected by using a CHI760D potentiostat with a Pt working and auxiliary electrodes, a

Ag/AgCl reference electrode, 1 mM solution of the compounds, and 0.10 M Bu₄NPF₆ (in THF or DCM) as electrolyte. Data for CV was obtained with a scan rate of 100 mV/s. Ferrocene was added at the end of each experiment and used as internal standard.

3.2.4 Syntheses

3.2.4.1 Synthesis of Mo₂(D^{m,p}AniF)₄ (5).

Mo₂(OAc)₄ (0.233 mmol, 0.100 g) and **1** (0.934 mmol, 0.239 g) were placed in THF (20mL). NaOCH₃/MeOH 0.5 M (1.87 mL) was added slowly to the reaction mixture under an ice bath. The reaction was allowed to reach room temperature and was stirred for 5h. THF was removed under reduced pressure. DCM (~ 25 mL) was added for extraction, and the resulting solution was filtered through frit-padded filter packed with celite. The filtrate was reduced in volume and then hexanes (40 mL) were added to precipitate a yellow powder. The precipitate was washed with EtOH (3 x 30mL) and Hex (2 x 30mL). Yield = 0.094 g, 33%. ¹H NMR δ (ppm in CDCl₃): 8.56 (s, 1H, NCHN-), 7.00 (t, 1H, aromatic C-H), 6.87 (d, 2H, aromatic C-H), 6.66, (d, 2H, aromatic C-H), 6.48 (d, 2H, aromatic C-H), 6.22 (s, 1H, aromatic C-H), 3.70 (s, 3H, -OCH₃), 3.51 (s, 3H, -OCH₃).

3.2.4.2 Synthesis of Mo₂(OAc)₂(Dipp^mAF)₂ (6).

Compound **2** (6.44 mmol, 2.0 g) was dissolved in THF (10 mL). MeLi/Et₂O 1.6 M solution (4 mL) was added slowly while having the reaction mixture in an ice bath. Once reached room temperature, the yellow reaction mixture was transferred to a flask containing a suspension of Mo₂(OAc)₄ (3.22 mmol, 1.38 g) in THF (10 mL). The reaction was stirred at room temperature for 5 h. Solvent was removed under reduced pressure to later extract with DCM. The red extracted solution was filtered through frit-padded a filter with celite. Solution volume was then reduced to ~3 mL under reduced pressure. EtOH (40 mL) was added and precipitated a yellow powder. The powder was washed with EtOH (3x30 mL) and Hex (2x30mL). Yield = 1.182 g, 40%. ¹H NMR δ

(ppm in CDCl₃): 8.13 (s, 1H, NCHN-), 7.13 (s, 3H, aromatic C-H), 7.02 (t, 1H, aromatic C-H), 6.53 (d, 1H, aromatic C-H), 6.37 (s, 1H, aromatic C-H), 6.26 (d, 1H, aromatic C-H), 3.66 (s, 1H, -OCH₃), 3.39 (sept., 2H, C-H), 2.71 (s, 3H, OAc C-H), 1.25 (d, 6H, C-H), 1.21 (d, 6H, C-H). ESI-MS (*m/z*): Calcd. 928.86 [ML], Found 931.83 [MLH⁺].

3.2.4.3 Synthesis of Mo₂(OAc)₂(*p*CIDippF)₂ (7).

Compound 3 (1.59 mmol, 0.500 g) was dissolved in THF (10 mL). NaOCH₃/MeOH 0.5 M solution (3.18 mL) was added slowly while having the reaction mixture in an ice bath. Once reached room temperature, the yellow reaction mixture was transferred to a flask containing a suspension of Mo₂(OAc)₄ (0.397 mmol, 0.170 g) in THF (5 mL). The reaction was stirred at room temperature for 5 h. Solvent was removed under reduced pressure to later extract with DCM. The extracted red solution was filtered through frit-padded a filter with celite. The volume of the solution was then reduced to ~3 mL under reduced pressure. EtOH (30 mL) was added and precipitated a yellow powder. The powder was washed with EtOH (3 x 30 mL) and Hex (2 x 30mL). Yield = 0.232 g, 42%. ¹H NMR δ (ppm in CDCl₃): 8.06 (s, 1H, NCHN-), 7.14 (t overlap with d, 3H, aromatic C-H), 7.09 (d, 2H, aromatic C-H), 6.64 (d, 2H, aromatic C-H), 3.34 (sept., 2H, C-H), 2.71 (s, 3H, OAc C-H), 1.23 (d, 6H, C-H), 1.20zz (d, 6H, C-H).

3.3 X-RAY CRYSTALLOGRAPHY

3.3.1 Mo₂(D^{m-p}AniF)₄

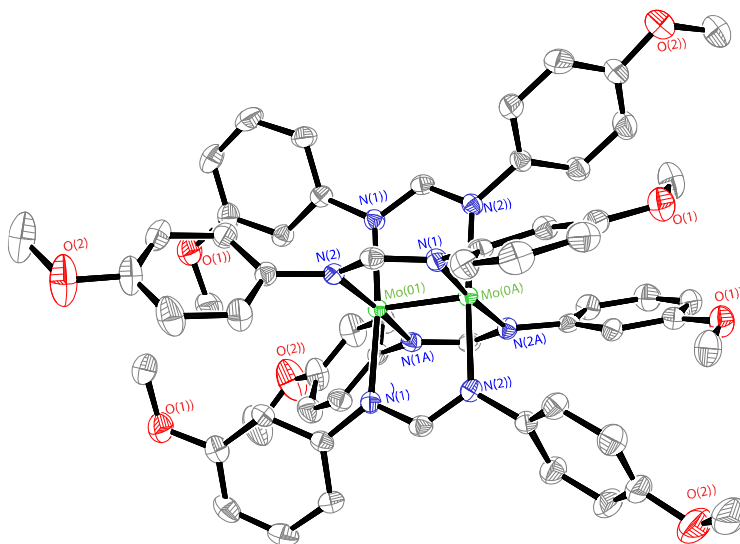


Figure 3.2. Crystal structure for **5** with ellipsoids drawn at 50% probability level.

A specimen of C₆₀H₆₀Mo₂N₈O₈ was used for the X-ray crystallography analysis. The X-ray intensity data were measured on a Bruker SMART APEX CCD system equipped with a fine-focus tube (MoK α , $\lambda = 0.71073$ Å) and a graphite monochromator. A total of 1440 frames were collected. The total exposure time was 12 hours. The frames were integrated with the Bruker SAINT software package using a narrow-frame algorithm. The integration of the data using a tetragonal unit cell yielded a total of 22915 reflections to a maximum θ angle of 27.55° (0.77 Å resolution), of which 3142 were independent (average redundancy 7.293, completeness = 99.5%, $R_{\text{int}} = 3.85\%$, $R_{\text{sig}} = 2.85\%$) and 2552 (81.22%) were greater than $2\sigma(F^2)$. The final cell constants of $\underline{a} = 19.2060(13)$ Å, $\underline{b} = 19.2060(13)$ Å, $\underline{c} = 14.8707(10)$ Å, volume = 5485.4(8) Å³, are based upon the refinement of the XYZ-centroids of reflections above $20\sigma(I)$. Data were corrected for absorption effects using the multi-scan method (SADABS).

The structure was solved and refined using the Bruker SHELXTL Software Package, using the space group I 41/a, with $Z = 4$ for the formula unit, $C_{60}H_{60}Mo_2N_8O_8$. The final anisotropic full-matrix least-squares refinement on F^2 with 179 variables converged at $R1 = 5.88\%$, for the observed data and $wR2 = 14.96\%$ for all data. The goodness-of-fit was 1.171. The largest peak in the final difference electron density synthesis was $1.932 \text{ e}^-/\text{\AA}^3$ and the largest hole was $-0.432 \text{ e}^-/\text{\AA}^3$ with an RMS deviation of $0.129 \text{ e}^-/\text{\AA}^3$. On the basis of the final model, the calculated density was 1.469 g/cm^3 and $F(000)$, 2496 e^- .

Table 3.1. X-ray crystallography data for **5**

Chemical formula	$C_{60}H_{60}Mo_2N_8O_8$
Formula weight	1213.04 g/mol
Temperature	100(2) K
Wavelength	0.71073 \AA
Crystal system	tetragonal
Space group	I 41/a
Unit cell dimensions	$a = 19.2060(13) \text{\AA}$ $b = 19.2060(13) \text{\AA}$ $\alpha = 90^\circ$ $c = 14.8707(10) \text{\AA}$ $\beta = 90^\circ$
Volume	$5485.4(8) \text{\AA}^3$ $\gamma = 90^\circ$
Z	4
Density (calculated)	1.469 g/cm^3
Absorption coefficient	0.521 mm^{-1}
$F(000)$	2496

3.3.2 Mo₂(OAc)₂(DippAF)₂

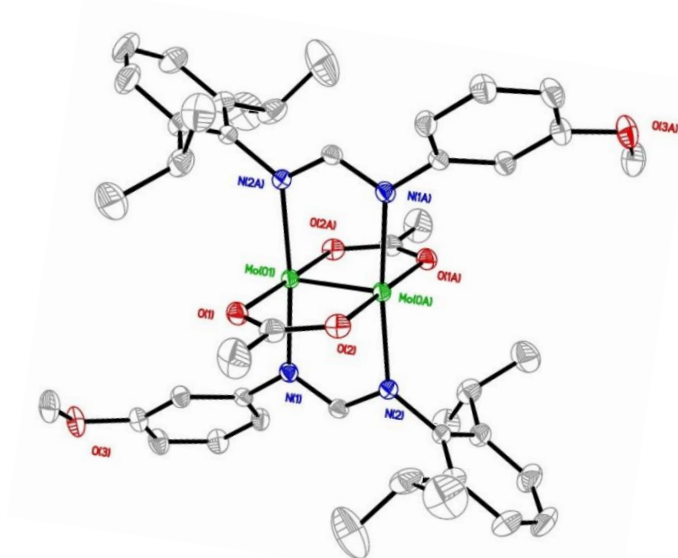


Figure 3.3. Crystal structure for **6** with ellipsoids drawn at 50% probability level.

A specimen of C₄₄H₅₆Mo₂N₄O₆, approximate dimensions 0.260 mm x 0.295 mm x 0.507 mm, was used for the X-ray crystallography analysis. The X-ray intensity data were measured on a Bruker SMART APEX CCD system equipped with a graphite monochromator and a MoK α fine-focus tube ($\lambda = 0.71073$ Å).

The total exposure time was 6 hours. The frames were integrated with the Bruker SAINT software package using a narrow-frame algorithm. The integration of the data using a triclinic unit cell yielded a total of 12800 reflections to a maximum θ angle of 27.56° (0.77 Å resolution), of which 5270 were independent (average redundancy 2.429, completeness = 98.6%, $R_{\text{int}} = 1.12\%$, $R_{\text{sig}} = 1.25\%$) and 5104 (96.85%) were greater than $2\sigma(F^2)$. The final cell constants of $\underline{a} = 10.3539(3)$ Å, $\underline{b} = 10.8756(3)$ Å, $\underline{c} = 11.5662(4)$ Å, $\beta = 82.9730(10)^\circ$, $\gamma = 72.2100(10)^\circ$, volume = 1153.92(6) Å³, are based upon the refinement of the XYZ-centroids of 9914 reflections above $20\sigma(I)$ with $5.272^\circ < 2\theta < 55.11^\circ$. Data were corrected for absorption effects using the multi-scan method (SADABS). The ratio of minimum to maximum apparent transmission was 0.920. The

calculated minimum and maximum transmission coefficients (based on crystal size) are 0.7540 and 0.8620. The squeeze method from Platon⁸⁴ was used, rendering a void of 112 Å³ with a residual electron count of 40e⁻ located at 0, 0, 0 (x, y, z).

The structure was solved and refined using the Bruker SHELXTL Software Package, using the space group P -1, with Z = 1 for the formula unit, C₄₄H₅₆Mo₂N₄O₆. The final anisotropic full-matrix least-squares refinement on F² with 258 variables converged at R1 = 2.11%, for the observed data and wR2 = 5.92% for all data. The goodness-of-fit was 1.099. The largest peak in the final difference electron density synthesis was 0.540 e⁻/Å³ and the largest hole was -0.718 e⁻/Å³ with an RMS deviation of 0.060 e⁻/Å³. On the basis of the final model, the calculated density was 1.337 g/cm³ and F(000), 480 e⁻.

Table 3.2. X-ray crystallography data for **6**.

Chemical formula	C ₄₄ H ₅₆ Mo ₂ N ₄ O ₆
Formula weight	928.80 g/mol
Temperature	150(2) K
Wavelength	0.71073 Å
Crystal size	0.260 x 0.295 x 0.507 mm
Crystal system	triclinic
Space group	P -1
Unit cell dimensions	a = 10.3539(3) Å b = 10.8756(3) Å α = 69° c = 11.5662(4) Å β = 82.9730(10)° γ =
Volume	1153.92(6) Å ³ 72.2100(10)°
Z	1
Density (calculated)	1.337 g/cm ³
Absorption coefficient	0.591 mm ⁻¹
F(000)	480

3.4 RESULTS AND DISCUSSION

3.4.1 Syntheses and Structures

Dimolybdenum complexes were prepared with $\text{Mo}_2(\text{OAc})_4$ as the starting material, where acetate ligands present in the bimetallic precursor were replaced by formamidinates.^{59,78} In the case of **5**, alternative synthesis can be done by utilizing $\text{Mo}(\text{CO})_6$ as a starting material, but the corresponding formamidine is added to the mixture instead of acetic acid.^{85,86} Upon substitution, $\text{Mo}_2(\text{OAc})_4 \cdot n(\text{L})_n$ solubilizes and the reaction mixture turns dark. Dichloromethane was utilized to extract the product and leave the Li or Na salt behind. Ethanol and hexanes were used for precipitation because this type of dimolybdenum compounds are known to be insoluble in these solvents. The obtained isomers maintained the same electron density in the metal centers. Yields for all compounds were expected to be higher, but possible formation of other structural isomers and monomers might have decreased it. Nonetheless, ^1H NMR for **6** and **7** depict the presence of a single isomer. Crystals for **5** (Figure 3.2) and **6** (Figure 3.3) were grown by layering DCM/Hex.

Table 3.3. Selected bond lengths (Å) and bond angles (°) for **5** and **6**.

	5	6
Mo1– Mo1	2.0991(9)	2.1009(2)
Mo1 – N1 (<i>m</i>)	2.154(3)	2.1422(12)
Mo1 – N2 (<i>p</i> , <i>i</i> -Pr)	2.169(3)	2.1643(12)
N1 – C1	1.327(5)	1.3252(19)
N2 – C1	1.322(5)	1.3264(18)
Mo1 – Mo1 – N1	93.21(9)	92.86(3)
Mo1 – Mo1 – N2	92.17(9)	92.66(3)
N1 – Mo1 – N2	89.49(13)	174.36(4)
N1 – C1 – N2	120.71(4)	121.07(13)

Metal-metal bond distances for **5** and **6** are on the range of quadrupole dimolybdenum bonds (2.06 – 2.17 Å),⁸⁷ with 2.0991 Å and 2.1009 Å respectively, as shown in Table 3.3. Molecules of this paddlewheel architecture are conventionally denominated as D_{4h} structures due

to the point group symmetry of symmetric tetrakis-ligated complexes. For symmetric tetrakis-ligated, *trans*-(2,2)-bis-substituted complexes, a D_{2h} symmetry is obtained. D_{4h} would be accurate to describe compound **5**, while D_{2h} would be an adequate description for **6** and **7** if the substituent groups were the same on both sides of the formamidates. However, the presence of our unsymmetric ligands produces the appearance of less symmetry elements. Hence, lower symmetry point groups represent them best, namely C_{2v} for **5** and C_{2h} for **6** and **7**.

3.4.2 Electrochemistry

Cyclic voltammetry on **5** reveals a one-electron reversible redox event at -0.240 V ($E_{1/2}$) vs Fc/Fc⁺. Figure 3.4 compares **5** versus its symmetric isomers. Redox events of $Mo_2(D^pAniF)_4$ and $Mo_2(D^mAniF)_4$ appear at -0.282 V and -0.190 V, respectively. The average $E_{1/2}$ for $Mo_2(D^pAniF)_4$ and $Mo_2(D^mAniF)_4$ is -0.236 V which is only a 4 mV difference with the experimental value obtained for **5**. It is observed that changing the position of one of the substituents in the phenyl ring, systematically affects the redox behavior of the system. Figure 3.5 depicts the dependence of $E_{1/2}$ to the Hammett constant (σ). The corresponding experimental and theoretical values obtained for **5** can be predicted with aid of Hammett constants. If the redox potentials for the symmetric versions are known, the redox event for the unsymmetric complex can be calculated in proportion to the average of the respective σ (See Chapter 2, Table 2.4).

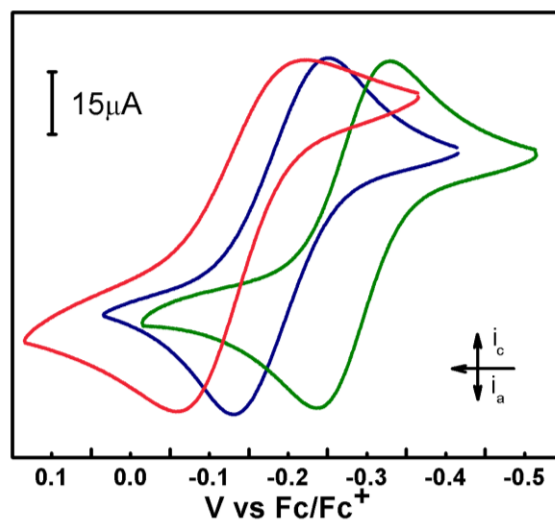


Figure 3.4 CV comparison of $\text{Mo}_2(\text{D}^m\text{AniF})_4$ (red, left), $\text{Mo}_2(\text{D}^{m,p}\text{AniF})_4$ (**5**) (blue, middle), and $\text{Mo}_2(\text{D}^p\text{AniF})_4$ (green, right).

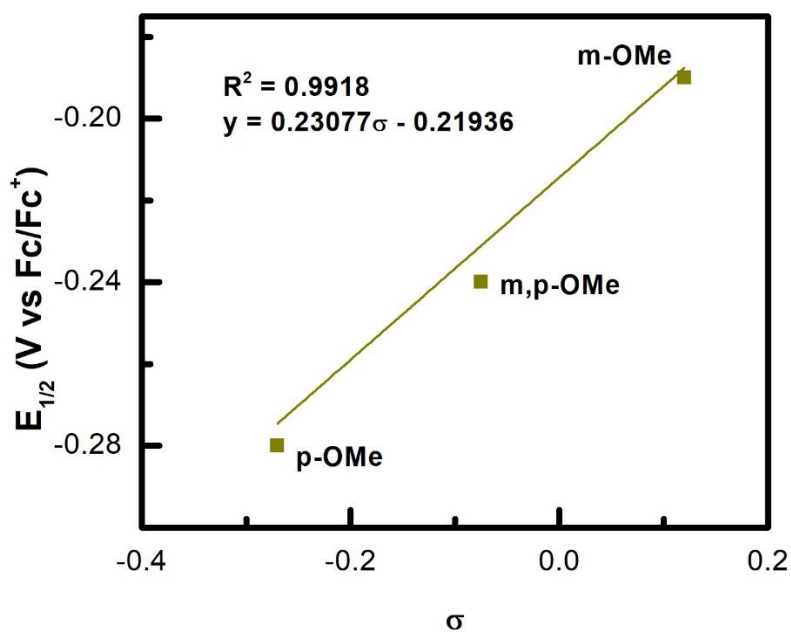


Figure 3.5 Hammett plot of **5** and its symmetric homologues.

Compounds **6** (Figure 3.6) and **7** (Figure 3.7) display a single reversible wave at -0.283 V and -0.260 V, respectively, in their cyclic voltammograms. As for similar compounds, the redox wave is assigned as a one-electron reversible redox event of $\text{Mo}_2^{4+/5+}$. Redox potentials for these

two compounds are close to each other varying by 23 mV. It comes to no surprise that they have such proximity since their average σ are also proximate to each other with -0.06 for **6** and -0.023 for **7**. For both systems, the trend follows that as σ becomes more negative, the dinuclear compounds also decrease their redox potential. Experimental unsymmetric variation of the second coordination sphere and predictive power of Hammett plots can be combined to comprehend a resourceful redox tuning tool.

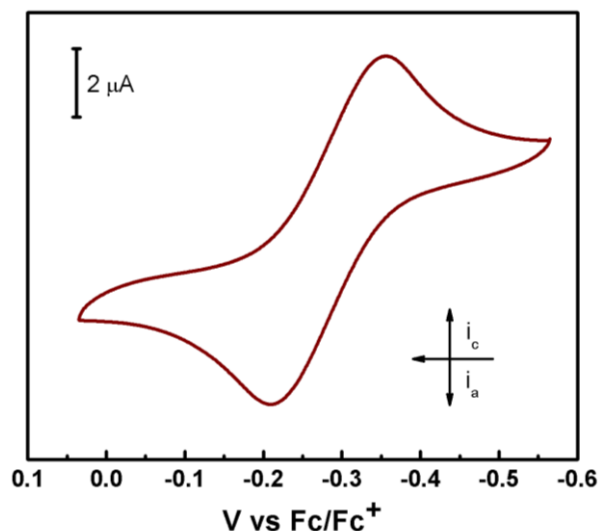


Figure 3.6. Cyclic voltammogram for **6**.

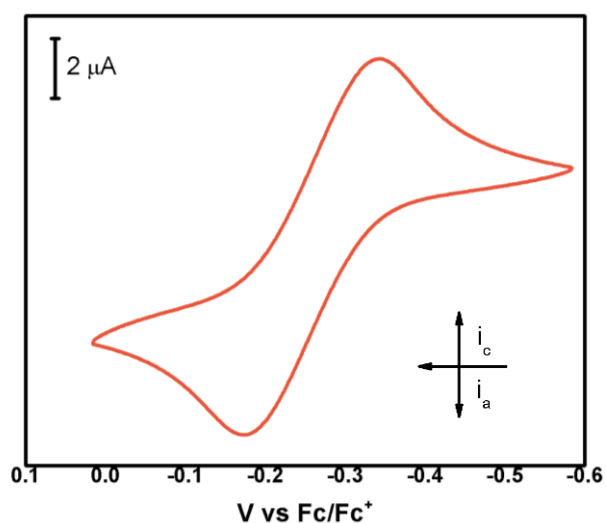
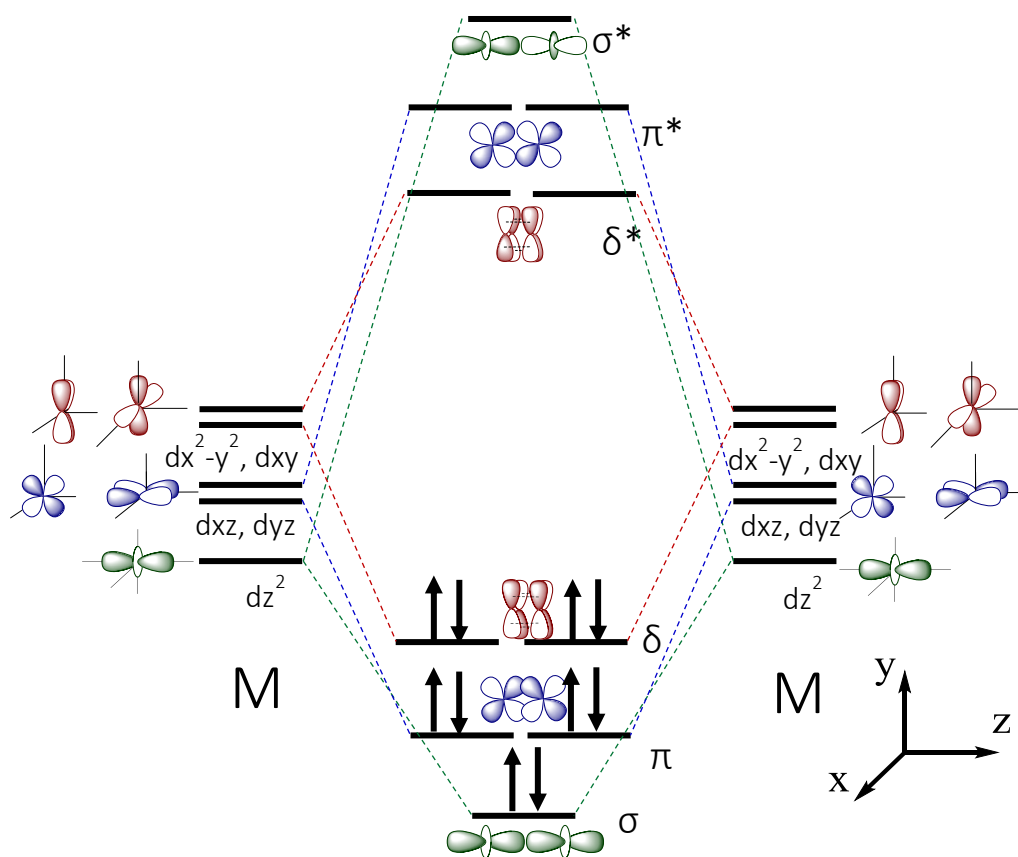


Figure 3.7. Cyclic voltammogram for **7**.

3.5 CONCLUSION

The formation of the discussed (2,2) isomers provided information about the electronic tuning process in bimetallic complexes. Dimolybdenum formamidinato complexes occurred by ligand substitution. All dinuclear centers discussed here present a single one-electron reversible redox event in their respective cyclic voltammograms. Binding unsymmetric ligands lowers the virtual symmetry of our systems and provides a plethora of substituent group combinations for electronic tuning. The tetrakis- substituted complex, **5**, was fully characterized and studied through electrochemistry. The comparison to its symmetric analogs demonstrated that it is possible to tune

the electronic properties of the complexes just by changing the position of a substituent in the phenyl ring by observing that the $E_{1/2}$ of **5** resulted to be between the *para*- and *meta*- versions of the complex. Redox potentials and Hammett constants for **6** and **7** have similar values. This relation supports the statement of tuning electronically dimolybdenum via remote substitution with unsymmetric formamidinate ligands.



Scheme 3.4. Molecular Orbital diagram (d-orbitals) of a quintuply bonded compound.

Although these dimolybdenum complexes correspond to the saturated D_{4h} paddlewheel structure, the acquired knowledge of electronic tuning in bimetallic systems can be transferred to other paddlewheel architectures, including D_{2h} . This insight can be transposed because the molecular orbital manifolds for these two systems (Scheme 3.2 and Scheme 3.4) are analogous, with the only

difference that the D_{2h} manifold has the availability of its $d_{x^2-y^2}$ orbitals to form a δ interaction between the two metal centers instead of occupying them in the metal-ligand interactions, as in the saturated D_{4h} systems. Quintuply bonded complexes have been reported in the case of dimolybdenum with D_{2h} symmetry containing open coordination sites and they are supported by bulky aryl formamidines.⁸⁸ These compounds are of interest since they offer reactivity and potential small molecule activation.^{56,89,90} Moreover, the bulkiness in the formamidinate ligands from **6** and **7** can support the D_{2h} structure and react them with H_2 to substitute the acetate ligands and expose the dinuclear compound to UV light to form a quintuple bond and hydrogen gas, as reported by Carmona.⁹¹ Alternative routes can be explored by synthesizing chlorinated dimolybdenum D_{4h} structures and reduce them to D_{2h} systems, as shown by Tsai.⁹² Saturated bimetallic complexes serve as platforms to understand unsaturated dinuclear compounds, especially molybdenum since it is one of the few elements who has shown homonuclear quintuple bonds, and higher bond orders offer new chemistry.

Chapter 4: Conclusion

In this thesis, unsymmetric aryl formamidinate ligands were utilized to tune the electronic behavior of dimolybdenum paddlewheel complexes. Unsymmetric formamidines were synthesized and characterized to later be used as ligands to form bimetallic complexes. Mo_2^{4+} compounds were synthesized, characterized and studied electrochemically. The effect of remote substitution of aryl formamidinates was investigated in dimolybdenum systems by synthetically lowering the symmetry. The direct relation of the second coordination sphere to redox behavior was observed, and it can be used as a tool to predict redox potentials and to further design complexes with specific electronic properties.

In Chapter 2, we were able to synthesize and characterize unsymmetric aryl formamidinates. Compound **1** was compared to its symmetric homologues. Preparation of **2** and **3** was approached by stepwise synthesis using DippFm as a precursor and were characterized successfully. Through x-ray crystallography, we determined that the N=C bonds in unsymmetric aryl formamidines will be positioned on the side of the more electron donating substituent. Furthermore, we propose a method for estimating σ values for unsymmetric formamidines, or disubstituted aryl rings in general.

In Chapter 3, synthesis, characterization, and electrochemical studies of dimolybdenum complexes were accomplished in order to observe the change in electronic properties caused by varying the second coordination sphere. Cyclic voltammetry of **5-7** revealed a one-electron reversible redox event. From comparing **5** versus its symmetric isomers, it was observed that the experimental value for $E_{1/2}$ agrees with the expected value. It was proved that changing the position of one of the substituents in the aromatic ring affected systematically the redox potential of the system. In addition, Hammett constants can be used as predictive tools when varying the

substituent groups of aryl formamidines, and likely other similar ligands, for electronic tuning purposes. The relation between redox potentials for **6** and **7** and their average σ supports the trend that as σ tends to be more negative, the redox potential of dimolybdenum compounds also decrease. Unsymmetric addition tool must hold to other dinuclear compounds if electronic tuning studies have been successfully done in other bimetallic systems. This study expands to compounds with open coordination sites, and these systems could be further reduced to explore reactivity.^{91,93} Unsymmetric combination of substituents and aligned to Hammett plots behavior can become a resourceful electronic tuning tool and gives a step forward towards manipulating meta-metal interactions.

Electronic tuning in saturated dimolybdenum systems give fundamental insights to apply that knowledge into sustainable energy production. Although unsymmetric formamidinato dimolybdenum complexes have a saturated architecture, unsymmetric ligand designing for redox tuning must hold to other paddlewheel dinuclear compounds, such as D_{2h} , since the molecular orbital manifolds for these systems are homologous, except for the participation of $d_{x^2-y^2}$ orbitals in δ bonding instead of metal-ligand interactions. The removal of two ligands in D_{2h} architecture provides open coordination sites which gives the opportunity for reactivity. In the case of dimolybdenum and dichromium analogs, complexes with open coordination and bond order of five, they have reacted with several reagents.^{56,94–101} Although these reagents are relatively highly reactive, bulky bisformamidinato dimolybdenum complexes like **6** and **7**, showed interconversion of bond order of four and five by oxidative addition and reductive elimination of dihydrogen.^{91,93} This reactivity suggests potential for small molecule activation through homogeneous catalysis. Furthermore, the high d-orbital overlap in dimolybdenum systems may resemble the interaction between two metal centers in metal-metal cooperativity in a surface. This relationship is important

because the information acquired from these dimolybdenum systems can be utilized to understand and even manipulate systematically what happens at the surface level. Molybdenum bimetallic complexes were used as platforms to understand unsaturated dinuclear compounds, especially molybdenum since it is one of the few elements who has shown homonuclear quintuple bonds with higher bond orders that offer new chemistry to promote small molecule activation relevant for sustainable energy production.

References

- (1) Lewis, N. S.; Nocera, D. G. Powering the Planet: Chemical Challenges in Solar Energy Utilization. *Proc. Natl. Acad. Sci.* **2006**, *103* (43), 15729–15735. <https://doi.org/10.1073/pnas.0603395103>.
- (2) Seh, Z. W.; Kibsgaard, J.; Dickens, C. F.; Chorkendorff, I.; Nørskov, J. K.; Jaramillo, T. F. Combining Theory and Experiment in Electrocatalysis: Insights into Materials Design. *Science* **2017**, *355* (6321). <https://doi.org/10.1126/science.aad4998>.
- (3) Gray, H. B. Powering the Planet with Solar Fuel. *Nat. Chem.* **2009**, *1* (1), 7–7. <https://doi.org/10.1038/nchem.141>.
- (4) Hunter, B. M.; Gray, H. B.; Müller, A. M. Earth-Abundant Heterogeneous Water Oxidation Catalysts. *Chem. Rev.* **2016**, *116* (22), 14120–14136. <https://doi.org/10.1021/acs.chemrev.6b00398>.
- (5) Hoffert, M. I.; Caldeira, K.; Jain, A. K.; Haites, E. F.; Harvey, L. D. D.; Potter, S. D.; Schlesinger, M. E.; Schneider, S. H.; Watts, R. G.; Wigley, T. M. L.; et al. Energy Implications of Future Stabilization of Atmospheric CO₂ Content. *Nature* **1998**, *395* (6705), 881–884. <https://doi.org/10.1038/27638>.
- (6) Lewis, N. S.; Crabtree, G. *Basic Research Needs for Solar Energy Utilization: Report of the Basic Energy Sciences Workshop on Solar Energy Utilization, April 18-21, 2005*; Lewis, N. S., Crabtree, G., Nozik, A. J., Wasielewski, M. R., Alivisatos, P., Eds.; US Department of Energy, Office of Basic Energy Science: Washington, DC, 2005.
- (7) Ataeivarjovi, E.; Tang, Z.; Chen, J. Study on CO₂ Desorption Behavior of a PDMS–SiO₂ Hybrid Membrane Applied in a Novel CO₂ Capture Process. *ACS Appl. Mater. Interfaces* **2018**, *10* (34), 28992–29002. <https://doi.org/10.1021/acsami.8b08630>.
- (8) Davis, S. J.; Caldeira, K.; Matthews, H. D. Future CO₂ Emissions and Climate Change from Existing Energy Infrastructure. *Science* **2010**, *329* (5997), 1330–1333. <https://doi.org/10.1126/science.1188566>.
- (9) Kapilashrami, M.; Zhang, Y.; Liu, Y.-S.; Hagfeldt, A.; Guo, J. Probing the Optical Property and Electronic Structure of TiO₂ Nanomaterials for Renewable Energy Applications. *Chem. Rev.* **2014**, *114* (19), 9662–9707. <https://doi.org/10.1021/cr5000893>.
- (10) Walter, M. G.; Warren, E. L.; McKone, J. R.; Boettcher, S. W.; Mi, Q.; Santori, E. A.; Lewis, N. S. Solar Water Splitting Cells. *Chem. Rev.* **2010**, *110* (11), 6446–6473. <https://doi.org/10.1021/cr1002326>.
- (11) Sivula, K.; Le Formal, F.; Grätzel, M. Solar Water Splitting: Progress Using Hematite (α -Fe(2) O(3)) Photoelectrodes. *ChemSusChem* **2011**, *4* (4), 432–449. <https://doi.org/10.1002/cssc.201000416>.
- (12) Dempsey, J. L.; Esswein, A. J.; Manke, D. R.; Rosenthal, J.; Soper, J. D.; Nocera, D. G. Molecular Chemistry of Consequence to Renewable Energy. *Inorg. Chem.* **2005**, *44* (20), 6879–6892. <https://doi.org/10.1021/ic0509276>.
- (13) Dresselhaus, M. S.; Thomas, I. L. Alternative Energy Technologies. *Nature* **2001**, *414* (6861), 332–337. <https://doi.org/10.1038/35104599>.
- (14) Balzani, V.; Credi, A.; Venturi, M. Photochemical Conversion of Solar Energy. *ChemSusChem* **2008**, *1* (1–2), 26–58. <https://doi.org/10.1002/cssc.200700087>.
- (15) Bloor, L. G.; Solarska, R.; Bienkowski, K.; Kulesza, P. J.; Augustynski, J.; Symes, M. D.; Cronin, L. Solar-Driven Water Oxidation and Decoupled Hydrogen Production Mediated

- by an Electron-Coupled-Proton Buffer. *J. Am. Chem. Soc.* **2016**, *138* (21), 6707–6710. <https://doi.org/10.1021/jacs.6b03187>.
- (16) Cook, T. R.; Dogutan, D. K.; Reece, S. Y.; Surendranath, Y.; Teets, T. S.; Nocera, D. G. Solar Energy Supply and Storage for the Legacy and Nonlegacy Worlds. *Chem. Rev.* **2010**, *110* (11), 6474–6502. <https://doi.org/10.1021/cr100246c>.
- (17) Turner, J. A. Sustainable Hydrogen Production. *Science* **2004**, *305* (5686), 972–974. <https://doi.org/10.1126/science.1103197>.
- (18) Gao, M.-R.; Liang, J.-X.; Zheng, Y.-R.; Xu, Y.-F.; Jiang, J.; Gao, Q.; Li, J.; Yu, S.-H. An Efficient Molybdenum Disulfide/Cobalt Diselenide Hybrid Catalyst for Electrochemical Hydrogen Generation. *Nat. Commun.* **2015**, *6* (1), 1–7. <https://doi.org/10.1038/ncomms6982>.
- (19) Nocera, D. G. The Artificial Leaf. *Acc. Chem. Res.* **2012**, *45* (5), 767–776. <https://doi.org/10.1021/ar2003013>.
- (20) York, A. P. E.; Xiao, T.; Green, M. L. H. Brief Overview of the Partial Oxidation of Methane to Synthesis Gas. *Top. Catal.* **2003**, *22* (3), 345–358. <https://doi.org/10.1023/A:1023552709642>.
- (21) Kawamura, F.; Taniguchi, T. Synthesis of Ammonia Using Sodium Melt. *Sci. Rep.* **2017**, *7* (1), 1–4. <https://doi.org/10.1038/s41598-017-12036-9>.
- (22) Hod, I.; Sampson, M. D.; Deria, P.; Kubiak, C. P.; Farha, O. K.; Hupp, J. T. Fe-Porphyrin-Based Metal–Organic Framework Films as High-Surface Concentration, Heterogeneous Catalysts for Electrochemical Reduction of CO₂. *ACS Catal.* **2015**, *5* (11), 6302–6309. <https://doi.org/10.1021/acscatal.5b01767>.
- (23) Kalz, K. F.; Kraehnert, R.; Dvoyashkin, M.; Dittmeyer, R.; Gläser, R.; Krewer, U.; Reuter, K.; Grunwaldt, J. Future Challenges in Heterogeneous Catalysis: Understanding Catalysts under Dynamic Reaction Conditions. *Chemcatchem* **2017**, *9* (1), 17–29. <https://doi.org/10.1002/cctc.201600996>.
- (24) Grunwaldt, J.-D.; Basini, L.; Clausen, B. S. In Situ EXAFS Study of Rh/Al₂O₃ Catalysts for Catalytic Partial Oxidation of Methane. *J. Catal.* **2001**, *200* (2), 321–329. <https://doi.org/10.1006/jcat.2001.3211>.
- (25) Hansen, P. L.; Wagner, J. B.; Helveg, S.; Rostrup-Nielsen, J. R.; Clausen, B. S.; Topsøe, H. Atom-Resolved Imaging of Dynamic Shape Changes in Supported Copper Nanocrystals. *Science* **2002**, *295* (5562), 2053–2055. <https://doi.org/10.1126/science.1069325>.
- (26) Kuld, S.; Thorhauge, M.; Falsig, H.; Elkjær, C. F.; Helveg, S.; Chorkendorff, I.; Sehested, J. Quantifying the Promotion of Cu Catalysts by ZnO for Methanol Synthesis. *Science* **2016**, *352* (6288), 969–974. <https://doi.org/10.1126/science.aaf0718>.
- (27) van den Berg, R.; Prieto, G.; Korpershoek, G.; van der Wal, L. I.; van Bunningen, A. J.; Lægsgaard-Jørgensen, S.; de Jongh, P. E.; de Jong, K. P. Structure Sensitivity of Cu and CuZn Catalysts Relevant to Industrial Methanol Synthesis. *Nat. Commun.* **2016**, *7* (1), 1–7. <https://doi.org/10.1038/ncomms13057>.
- (28) Kimmerle, B.; Baiker, A.; Grunwaldt, J.-D. Oscillatory Behaviour of Catalytic Properties, Structure and Temperature during the Catalytic Partial Oxidation of Methane on Pd/Al₂O₃. *Phys. Chem. Chem. Phys.* **2010**, *12* (10), 2288–2291. <https://doi.org/10.1039/B924001B>.

- (29) Helveg, S.; Lopez-Cartes, C.; Sehested, J.; Hansen, P. L.; Clausen, B. S.; Rostrup-Nielsen, J. R.; Abild-Pedersen, F.; Norskov, J. K. Atomic-Scale Imaging of Carbon Nanofibre Growth. *Nature* **2004**, *427* (6973), 426–429. <https://doi.org/10.1038/nature02278>.
- (30) Yu, J.; Zhou, Y.; Hua, X.; Liu, S.; Zhu, Z.; Yu, X.-Y. Capturing the Transient Species at the Electrode–Electrolyte Interface by in Situ Dynamic Molecular Imaging. *Chem. Commun.* **2016**, *52* (73), 10952–10955. <https://doi.org/10.1039/C6CC02893D>.
- (31) Sabbe, M. K.; Reyniers, M.-F.; Reuter, K. First-Principles Kinetic Modeling in Heterogeneous Catalysis: An Industrial Perspective on Best-Practice, Gaps and Needs. *Catal. Sci. Technol.* **2012**, *2* (10), 2010–2024. <https://doi.org/10.1039/C2CY20261A>.
- (32) Nørskov, J. K.; Bligaard, T.; Rossmeisl, J.; Christensen, C. H. Towards the Computational Design of Solid Catalysts. *Nat. Chem.* **2009**, *1* (1), 37–46. <https://doi.org/10.1038/nchem.121>.
- (33) López, N.; Almora-Barrios, N.; Carchini, G.; Błoński, P.; Bellarosa, L.; García-Muelas, R.; Novell-Leruth, G.; García-Mota, M. State-of-the-Art and Challenges in Theoretical Simulations of Heterogeneous Catalysis at the Microscopic Level. *Catal. Sci. Technol.* **2012**, *2* (12), 2405–2417. <https://doi.org/10.1039/C2CY20384G>.
- (34) Muetterties, E. L. The Organometallic Chemistry of Metal Surfaces. *Pure Appl. Chem.* **1982**, *54* (1), 83–96. <https://doi.org/10.1351/pac198254010083>.
- (35) Marks, T. J. Surface-Bound Metal Hydrocarbyls. Organometallic Connections between Heterogeneous and Homogeneous Catalysis. *Acc. Chem. Res.* **1992**, *25* (2), 57–65. <https://doi.org/10.1021/ar00014a001>.
- (36) Torkelson, J. R.; Antwi-Nsiah, F. H.; McDonald, R.; Cowie, M.; Pruis, J. G.; Jalkanen, K. J.; DeKock, R. L. Metal–Metal Cooperativity Effects in Promoting C–H Bond Cleavage of a Methyl Group by an Adjacent Metal Center. *J. Am. Chem. Soc.* **1999**, *121* (15), 3666–3683. <https://doi.org/10.1021/ja983525o>.
- (37) Werner, H. Principles and Applications of Organotransition Metal Chemistry. Von J. P. Collman, L. G. Hegedus, J. R. Norton Und R. G. Finke. Oxford University Press, Oxford 1987. XII, 989 S., Geb. £ 40.00. – ISBN 0-935702-51-2. *Angew. Chem.* **1988**, *100* (8), 1145–1146. <https://doi.org/10.1002/ange.19881000838>.
- (38) Lynam, J. The Organometallic Chemistry of the Transition Metals, 6th Edition Robert H. Crabtree Wiley, 2014 520 Pages €80.40 £66.95 ISBN: 978-1-118-13807-6. *Appl. Organomet. Chem.* **2015**, *29* (1), 60–60. <https://doi.org/10.1002/aoc.3241>.
- (39) Bradley, J. S. Homogeneous Carbon Monoxide Hydrogenation to Methanol Catalyzed by Soluble Ruthenium Complexes. *J. Am. Chem. Soc.* **1979**, *101* (24), 7419–7421. <https://doi.org/10.1021/ja00518a056>.
- (40) Li, H.; Li, L.; Marks, T. J.; Liable-Sands, L.; Rheingold, A. L. Catalyst/Cocatalyst Nuclearity Effects in Single-Site Olefin Polymerization. Significantly Enhanced 1-Octene and Isobutene Comonomer Enchainment in Ethylene Polymerizations Mediated by Binuclear Catalysts and Cocatalysts. *J. Am. Chem. Soc.* **2003**, *125* (36), 10788–10789. <https://doi.org/10.1021/ja036289c>.
- (41) Wigginton, J. R.; Chokshi, A.; Graham, T. W.; McDonald, R.; Ferguson, M. J.; Cowie, M. Alkyne/Methylene Coupling Reactions at Adjacent Rh/Os Centers: Stepwise Transformations from C1- through C4-Bridged Species. *Organometallics* **2005**, *24* (26), 6398–6410. <https://doi.org/10.1021/om058041x>.
- (42) *Multiple Bonds between Metal Atoms*, 3rd ed.; Cotton, F. A., Murillo, C. A., Walton, R. A., Eds.; Springer-Verlag: New York, 2005. <https://doi.org/10.1007/b136230>.

- (43) Cotton, F. A.; Lei, P.; Murillo, C. A.; Wang, L.-S. Synthesis of Unsymmetrical Formamidines and Benzamidines: Structural Studies of Copper, Cobalt and Chromium Complexes. *Inorganica Chim. Acta* **2003**, *349*, 165–172. [https://doi.org/10.1016/S0020-1693\(03\)00092-6](https://doi.org/10.1016/S0020-1693(03)00092-6).
- (44) Harisomayajula, N. V. S.; Nair, A. K.; Tsai, Y.-C. Discovering Complexes Containing a Metal–Metal Quintuple Bond: From Theory to Practice. *Chem. Commun.* **2014**, *50* (26), 3391–3412. <https://doi.org/10.1039/C3CC48203K>.
- (45) Aparoy, P.; Kumar Reddy, K.; Reddanna, P. Structure and Ligand Based Drug Design Strategies in the Development of Novel 5-LOX Inhibitors. *Curr. Med. Chem.* **2012**, *19* (22), 3763–3778. <https://doi.org/10.2174/092986712801661112>.
- (46) Kulkarni, N. V.; Elkin, T.; Tumaniskii, B.; Botoshansky, M.; Shimon, L. J. W.; Eisen, M. S. Asymmetric Bis(Formamidinate) Group 4 Complexes: Synthesis, Structure and Their Reactivity in the Polymerization of α -Olefins. *Organometallics* **2014**, *33* (12), 3119–3136. <https://doi.org/10.1021/om500345r>.
- (47) Elsevier, C. J.; Reedijk, J.; Walton, P. H.; Ward, M. D. Ligand Design in Coordination Chemistry: Approaches to New Catalysts, New Materials, and a More Sustainable Environment. *Dalton Trans.* **2003**, No. 10, 1869–1880. <https://doi.org/10.1039/B303975G>.
- (48) Clérac, R.; Cotton, F. A.; Dunbar, K. R.; Murillo, C. A.; Wang, X. Dinuclear and Heteropolynuclear Complexes Containing Mo²⁴⁺ Units. *Inorg. Chem.* **2001**, *40* (3), 420–426. <https://doi.org/10.1021/ic001002n>.
- (49) Li, J.; Jiao, J.; Zhang, C.; Shi, M.; Zhang, J. Facile Syntheses of N-Heterocyclic Carbene Precursors through I₂- or NIS-Promoted Amidinium of N-Alkenyl Formamidines. *Chem. – Asian J.* **2016**, *11* (9), 1361–1365. <https://doi.org/10.1002/asia.201600182>.
- (50) Lin, C.; Protasiewicz, J. D.; Smith, E. T.; Ren, T. Redox Tuning of the Dimolybdenum Compounds at the Ligand Periphery: A Direct Correlation with the Hammett Constant of the Substituents. *J. Chem. Soc. Chem. Commun.* **1995**, No. 22, 2257–2258. <https://doi.org/10.1039/C39950002257>.
- (51) Lin, C.; Protasiewicz, J. D.; Smith, E. T.; Ren, T. Linear Free Energy Relationships in Dinuclear Compounds. 2. Inductive Redox Tuning via Remote Substituents in Quadruply Bonded Dimolybdenum Compounds. *Inorg. Chem.* **1996**, *35* (22), 6422–6428. <https://doi.org/10.1021/ic960555o>.
- (52) Lin, C.; Protasiewicz, J. D.; Ren, T. Electronic Tuning Using Remote Substituents in Tetrakis(μ -N,N'-Diarylformamidinato)Dinickel. Linear Free Energy Relationships in Dinuclear Compounds. 3. *Inorg. Chem.* **1996**, *35* (25), 7455–7458. <https://doi.org/10.1021/ic960842s>.
- (53) A survey of Hammett substituent constants and resonance and field parameters | Chemical Reviews <https://pubs.acs.org/doi/10.1021/cr00002a004> (accessed Dec 17, 2019).
- (54) The Effect of Structure upon the Reactions of Organic Compounds. Benzene Derivatives | Journal of the American Chemical Society <https://pubs.acs.org/doi/abs/10.1021/ja01280a022> (accessed Dec 17, 2019).
- (55) Rincón, L.; Almeida, R. Is the Hammett's Constant Free of Steric Effects? *J. Phys. Chem. A* **2012**, *116* (28), 7523–7530. <https://doi.org/10.1021/jp300160g>.
- (56) Tamne, E. S.; Noor, A.; Qayyum, S.; Bauer, T.; Kempe, R. Quintuple Bond Reactivity toward Group 16 and 17 Elements: Addition vs Insertion. *Inorg. Chem.* **2013**, *52* (1), 329–336. <https://doi.org/10.1021/ic3020805>.

- (57) McDANIEL, D. H.; BROWN, H. C. An Extended Table of Hammett Substituent Constants Based on the Ionization of Substituted Benzoic Acids. *J. Org. Chem.* **1958**, *23* (3), 420–427. <https://doi.org/10.1021/jo01097a026>.
- (58) Cotton, F. A.; Harris, C. B. The Crystal and Molecular Structure of Dipotassium Octachlorodirhenate(III) Dihydrate, $K_2 [Re_2 Cl_8] \cdot 2H_2O$. *Inorg. Chem.* **1965**, *4* (3), 330–333. <https://doi.org/10.1021/ic50025a015>.
- (59) *Multiple Bonds between Metal Atoms*, 3rd ed.; Cotton, F. A., Murillo, C. A., Walton, R. A., Eds.; Springer-Verlag: New York, 2005.
- (60) Collman, J. *Principles and Applications of Organotransition Metal Chemistry*; Mill Valley, CA, University Science Books, 1987.
- (61) Grubbs, R. H. *Homogeneous Catalysis: The Applications and Chemistry of Catalysis by Soluble Transition Metal Complexes*. By G. W. Parshall and S. D. Ittel, Wiley, New York, 342 Pp., 1992, \$50.00. *AIChE J.* **1993**, *39* (9), 1578–1578. <https://doi.org/10.1002/aic.690390919>.
- (62) Kochi, J. K. Electron Transfer and Charge Transfer: Twin Themes in Unifying the Mechanisms of Organic and Organometallic Reactions. *Angew. Chem. Int. Ed. Engl.* **1988**, *27* (10), 1227–1266. <https://doi.org/10.1002/anie.198812273>.
- (63) Cotton, F. A.; Daniels, L. M.; Murillo, C. A.; Timmons, D. J.; Wilkinson, C. C. The Extraordinary Ability of Guanidinate Derivatives to Stabilize Higher Oxidation Numbers in Dimetal Units by Modification of Redox Potentials: Structures of Mo^{25+} and Mo^{26+} Compounds. *J. Am. Chem. Soc.* **2002**, *124* (31), 9249–9256. <https://doi.org/10.1021/ja0266464>.
- (64) Lindsay, A. J.; Wilkinson, G.; Motevalli, M.; Hursthouse, M. B. Reactions of Tetra- μ -Carboxylato-Diruthenium(II,II) Compounds. X-Ray Crystal Structures of $Ru_2(\mu-O_2CCF_3)_4(Thf)_2$, $Ru_2(\mu-O_2CR)_4(NO)_2$ ($R = Et$ or CF_3), and $\{Na_3[Ru_2(\mu-O_2CO)_4] \cdot 6H_2O\}_n$. *J. Chem. Soc. Dalton Trans.* **1987**, No. 11, 2723–2736. <https://doi.org/10.1039/DT9870002723>.
- (65) Cotton, F. Albert.; Matusz, Marek.; Poli, Rinaldo.; Feng, Xuejun. Dinuclear Formamidinato Complexes of Nickel and Palladium. *J. Am. Chem. Soc.* **1988**, *110* (4), 1144–1154. <https://doi.org/10.1021/ja00212a024>.
- (66) Cotton, F. A.; Daniels, L. M.; Murillo, C. A. A Systematic Approach in the Preparation of Compounds with σ -Bonded Vanadium-to-Vanadium Triple Bonds: Synthesis, Reactivity, and Structural Characterization. *Inorg. Chem.* **1993**, *32* (13), 2881–2885. <https://doi.org/10.1021/ic00065a014>.
- (67) Cotton, F. A.; Daniels, L. M.; Matonic, J. H.; Murillo, C. A. Highly Distorted Diiron(II, II) Complexes Containing Four Amidinate Ligands. A Long and Short Metal-Metal Distance. *Inorganica Chim. Acta* **1997**, *256* (2), 277–282. [https://doi.org/10.1016/S0020-1693\(96\)05470-9](https://doi.org/10.1016/S0020-1693(96)05470-9).
- (68) Cotton, F. A.; Daniels, L. M.; Falvello, L. R.; Matonic, J. H.; Murillo, C. A. Trigonal-Lantern Dinuclear Compounds of Diiron(I,II): The Synthesis and Characterization of Two Highly Paramagnetic $Fe_2(AMIDINATO)_3$ Species with Short Metal-Metal Bonds. *Inorganica Chim. Acta* **1997**, *256* (2), 269–275. [https://doi.org/10.1016/S0020-1693\(96\)05469-2](https://doi.org/10.1016/S0020-1693(96)05469-2).
- (69) Cotton, F. A.; Daniels, L. M.; Feng, X.; Maloney, D. J.; Matonic, J. H.; Murilio, C. A. The Use of $CoCl_2(AMIDINE)_2$ Compounds in the Synthesis of Tetragonal Lantern Dicobalt Compounds: Synthesis, Structures and Theoretical Studies of $Co_2(DPhF)_4$ and the

- Oxidized Species $[\text{Co}_2(\text{DPhBz})_4]^+$ (DPhF = N,N'-Diphenylformamidinate, DPhBz = N,N'-Diphenylbenzamidinate). *Inorganica Chim. Acta* **1997**, *256* (2), 291–301. [https://doi.org/10.1016/S0020-1693\(96\)05472-2](https://doi.org/10.1016/S0020-1693(96)05472-2).
- (70) Klein, A.; Kaim, W.; Hornung, F. M.; Fiedler, J.; Zalis, S. Electronic and Molecular Structure of 2,2'-Bipyrimidine-Bridged Bis(Organoplatinum) Complexes in Various Oxidation States. Radical-Bridged Diplatinum Species and the Absence of a Pt(III)/Pt(II) Mixed-Valent Intermediate. *Inorganica Chim. Acta* **1997**, *264* (1), 269–278. [https://doi.org/10.1016/S0020-1693\(97\)05704-6](https://doi.org/10.1016/S0020-1693(97)05704-6).
- (71) Lin, C.; Protasiewicz, J. D.; Smith, E. T.; Ren, T. Linear Free Energy Relationships in Dinuclear Compounds. 2. Inductive Redox Tuning via Remote Substituents in Quadruply Bonded Dimolybdenum Compounds. *Inorg. Chem.* **1996**, *35* (22), 6422–6428. <https://doi.org/10.1021/ic960555o>.
- (72) Ren, T. Substituent Effects in Dinuclear Paddlewheel Compounds: Electrochemical and Spectroscopic Investigations. *Coord. Chem. Rev.* **1998**, *175* (1), 43–58. [https://doi.org/10.1016/S0010-8545\(98\)00202-1](https://doi.org/10.1016/S0010-8545(98)00202-1).
- (73) Yeo, C. I.; Ooi, K. K.; Tiekink, E. R. T. Gold-Based Medicine: A Paradigm Shift in Anti-Cancer Therapy? *Mol. J. Synth. Chem. Nat. Prod. Chem.* **2018**, *23* (6). <https://doi.org/10.3390/molecules23061410>.
- (74) Cayton, R. H.; Chisholm, M. H.; Huffman, J. C.; Lobkovsky, E. B. Metal-Metal Multiple Bonds in Ordered Assemblies. 1. Tetranuclear Molybdenum and Tungsten Carboxylates Involving Covalently Linked Metal-Metal Quadruple Bonds. Molecular Models for Subunits of One-Dimensional Stiff-Chain Polymers. *J. Am. Chem. Soc.* **1991**, *113* (23), 8709–8724. <https://doi.org/10.1021/ja00023a019>.
- (75) Das, R. K.; Saha, B.; Rahaman, S. M. W.; Bera, J. K. Bimetallic Catalysis Involving Dipalladium(I) and Diruthenium(I) Complexes. *Chem. – Eur. J.* **2010**, *16* (48), 14459–14468. <https://doi.org/10.1002/chem.201001960>.
- (76) Gray, T. G.; Veige, A. S.; Nocera, D. G. Cooperative Bimetallic Reactivity: Hydrogen Activation in Two-Electron Mixed-Valence Compounds. *J. Am. Chem. Soc.* **2004**, *126* (31), 9760–9768. <https://doi.org/10.1021/ja0491432>.
- (77) Lin, C.; Protasiewicz, J. D.; Ren, T. Electronic Tuning Using Remote Substituents in Tetrakis(μ -N,N'-Diarylformamidinato)Dinickel. Linear Free Energy Relationships in Dinuclear Compounds. 3. *Inorg. Chem.* **1996**, *35* (25), 7455–7458. <https://doi.org/10.1021/ic960842s>.
- (78) Lin, C.; Protasiewicz, J. D.; Smith, E. T.; Ren, T. Redox Tuning of the Dimolybdenum Compounds at the Ligand Periphery: A Direct Correlation with the Hammett Constant of the Substituents. *J. Chem. Soc. Chem. Commun.* **1995**, No. 22, 2257–2258. <https://doi.org/10.1039/C39950002257>.
- (79) Carlson-Day, K. M.; Eglin, J. L.; Lin, C.; Smith, L. T.; Staples, R. J.; Wipf, D. O. Synthesis of Multiply-Bonded Dichromium Complexes with a Variety of Formamidinate Ligands. *Polyhedron* **1999**, *18* (6), 817–824. [https://doi.org/10.1016/S0277-5387\(98\)00362-3](https://doi.org/10.1016/S0277-5387(98)00362-3).
- (80) Dolinar, B. S.; Berry, J. F. Lewis Acid Enhanced Axial Ligation of $[\text{Mo}_2]^{4+}$ Complexes. *Inorg. Chem.* **2013**, *52* (8), 4658–4667. <https://doi.org/10.1021/ic400275x>.
- (81) Dolinar, B. S.; Berry, J. F. Influence of Lewis Acid Charge and Proximity in $\text{MoMo}\cdots\text{M}$ Linear Chain Compounds with $\text{M}=\text{Na}^+$, Ca^{2+} , Sr^{2+} , and Y^{3+} . *Polyhedron* **2016**, *103*, 71–78. <https://doi.org/10.1016/j.poly.2015.09.028>.

- (82) Pence, L. E.; Weisgerber, A. M.; Maounis, F. A. Synthesis of Molybdenum-Molybdenum Quadruple Bonds: A Multistep Advanced Synthesis Laboratory Experiment. *J. Chem. Educ.* **1999**, *76* (3), 404. <https://doi.org/10.1021/ed076p404>.
- (83) Wu, Y.-Y.; Yeh, C.-W.; Chan, Z.-K.; Lin, C.-H.; Yang, C.-H.; Chen, J.-D.; Wang, J.-C. Chemistry of Dimolybdenum Complexes Containing Bridging Anions of N,N'-Di(3-Methoxyphenyl)Formamidine. *J. Mol. Struct.* **2008**, *890* (1), 48–56. <https://doi.org/10.1016/j.molstruc.2008.01.037>.
- (84) Spek, A. L. Structure Validation in Chemical Crystallography. *Acta Crystallogr. D Biol. Crystallogr.* **2009**, *65* (2), 148–155. <https://doi.org/10.1107/S090744490804362X>.
- (85) Brignole, A. B.; Cotton, F. A.; Dori, Z.; Dori, Z.; Dori, Z.; Wilkinson, G. Rhenium and Molybdenum Compounds Containing Quadruple Bonds. In *Inorganic Syntheses*; John Wiley & Sons, Ltd, 2007; pp 81–89. <https://doi.org/10.1002/9780470132449.ch15>.
- (86) Cotton, F. A.; Donahue, J. P.; Hall, M. B.; Murillo, C. A.; Villagrán, D. Reaction Products of W(CO)₆ with Formamidines; Electronic Structure of a W₂(μ-CO)₂ Core with Unsymmetric Bridging Carbonyls. *Inorg. Chem.* **2004**, *43* (22), 6954–6964. <https://doi.org/10.1021/ic049116c>.
- (87) Cotton, F. A.; Daniels, L. M.; Hillard, E. A.; Murillo, C. A. The Lengths of Molybdenum to Molybdenum Quadruple Bonds: Correlations, Explanations, and Corrections. *Inorg. Chem.* **2002**, *41* (9), 2466–2470. <https://doi.org/10.1021/ic025508c>.
- (88) Nair, A. K.; Harisomayajula, N. V. S.; Tsai, Y.-C. Theory, Synthesis and Reactivity of Quintuple Bonded Complexes. *Dalton Trans.* **2014**, *43* (15), 5618–5638. <https://doi.org/10.1039/C3DT53565G>.
- (89) Nair, A. K.; Harisomayajula, N. V. S.; Tsai, Y.-C. The Lengths of the Metal-to-Metal Quintuple Bonds and Reactivity Thereof. *Inorganica Chim. Acta* **2015**, *424*, 51–62. <https://doi.org/10.1016/j.ica.2014.09.020>.
- (90) Chen, Y.; Sakaki, S. Mo–Mo Quintuple Bond Is Highly Reactive in H–H, C–H, and O–H σ-Bond Cleavages Because of the Polarized Electronic Structure in Transition State. *Inorg. Chem.* **2017**, *56* (7), 4011–4020. <https://doi.org/10.1021/acs.inorgchem.6b03103>.
- (91) Carrasco, M.; Curado, N.; Maya, C.; Peloso, R.; Rodríguez, A.; Ruiz, E.; Alvarez, S.; Carmona, E. Interconversion of Quadruply and Quintuply Bonded Molybdenum Complexes by Reductive Elimination and Oxidative Addition of Dihydrogen. *Angew. Chem. Int. Ed.* **2013**, *52* (11), 3227–3231. <https://doi.org/10.1002/anie.201209064>.
- (92) Tsai, Y.-C.; Chen, H.-Z.; Chang, C.-C.; Yu, J.-S. K.; Lee, G.-H.; Wang, Y.; Kuo, T.-S. Journey from Mo–Mo Quadruple Bonds to Quintuple Bonds. *J. Am. Chem. Soc.* **2009**, *131* (35), 12534–12535. <https://doi.org/10.1021/ja905035f>.
- (93) Curado, N.; Carrasco, M.; Álvarez, E.; Maya, C.; Peloso, R.; Rodríguez, A.; López-Serrano, J.; Carmona, E. Lithium Di- and Trimethyl Dimolybdenum(II) Complexes with Mo–Mo Quadruple Bonds and Bridging Methyl Groups. *J. Am. Chem. Soc.* **2015**, *137* (38), 12378–12387. <https://doi.org/10.1021/jacs.5b07899>.
- (94) Noor, A.; Glatz, G.; Müller, R.; Kaupp, M.; Demeshko, S.; Kempe, R. Carboalumination of a Chromium–Chromium Quintuple Bond. *Nat. Chem.* **2009**, *1* (4), 322–325. <https://doi.org/10.1038/nchem.255>.
- (95) Ni, C.; Ellis, B. D.; Long, G. J.; Power, P. P. Reactions of Ar'CrCrAr' with N₂O or N₃(1-Ad): Complete Cleavage of the Cr–Cr Quintuple Interaction. *Chem. Commun.* **2009**, No. 17, 2332–2334. <https://doi.org/10.1039/B901494B>.

- (96) Wu, P.-F.; Liu, S.-C.; Shieh, Y.-J.; Kuo, T.-S.; Lee, G.-H.; Wang, Y.; Tsai, Y.-C. Divergent Reactivity of Nitric Oxide with Metal–Metal Quintuple Bonds. *Chem. Commun.* **2013**, *49* (39), 4391–4393. <https://doi.org/10.1039/C3CC37118B>.
- (97) Schwarzmaier, C.; Noor, A.; Glatz, G.; Zabel, M.; Timoshkin, A. Y.; Cossairt, B. M.; Cummins, C. C.; Kempe, R.; Scheer, M. Formation of Cyclo-E42– Units (E4=P4, As4, AsP3) by a Complex with a Cr□Cr Quintuple Bond. *Angew. Chem. Int. Ed.* **2011**, *50* (32), 7283–7286. <https://doi.org/10.1002/anie.201102361>.
- (98) Noor, A.; Sobgwi Tamne, E.; Qayyum, S.; Bauer, T.; Kempe, R. Cycloaddition Reactions of a Chromium–Chromium Quintuple Bond. *Chem. – Eur. J.* **2011**, *17* (25), 6900–6903. <https://doi.org/10.1002/chem.201100841>.
- (99) Shen, J.; Yap, G. P. A.; Werner, J.-P.; Theopold, K. H. Reactions of a Quintuply Bonded Chromium Dimer with Alkynes. *Chem. Commun.* **2011**, *47* (44), 12191–12193. <https://doi.org/10.1039/C1CC15218A>.
- (100) Chen, H.-Z.; Liu, S.-C.; Yen, C.-H.; Yu, J.-S. K.; Shieh, Y.-J.; Kuo, T.-S.; Tsai, Y.-C. Reactions of Metal–Metal Quintuple Bonds with Alkynes: [2+2+2] and [2+2] Cycloadditions. *Angew. Chem. Int. Ed.* **2012**, *51* (41), 10342–10346. <https://doi.org/10.1002/anie.201205027>.
- (101) Chen, H.-G.; Hsueh, H.-W.; Kuo, T.-S.; Tsai, Y.-C. Haloacylation of the Quintuple-Bonded Group VI Metal Amidinate Dimers and Disproportionation of Acyl Groups to Form Carbynes. *Angew. Chem. Int. Ed.* **2013**, *52* (39), 10256–10260. <https://doi.org/10.1002/anie.201304750>.

Appendix

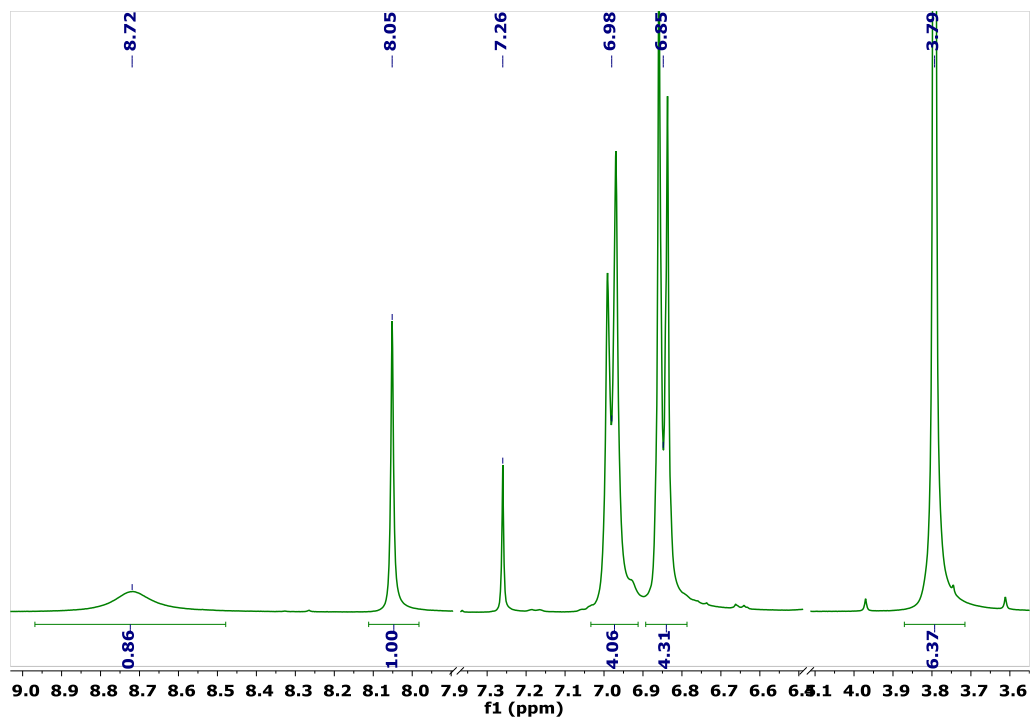


Figure A.1. ¹H NMR spectrum of D^pAniF vs CDCl₃.

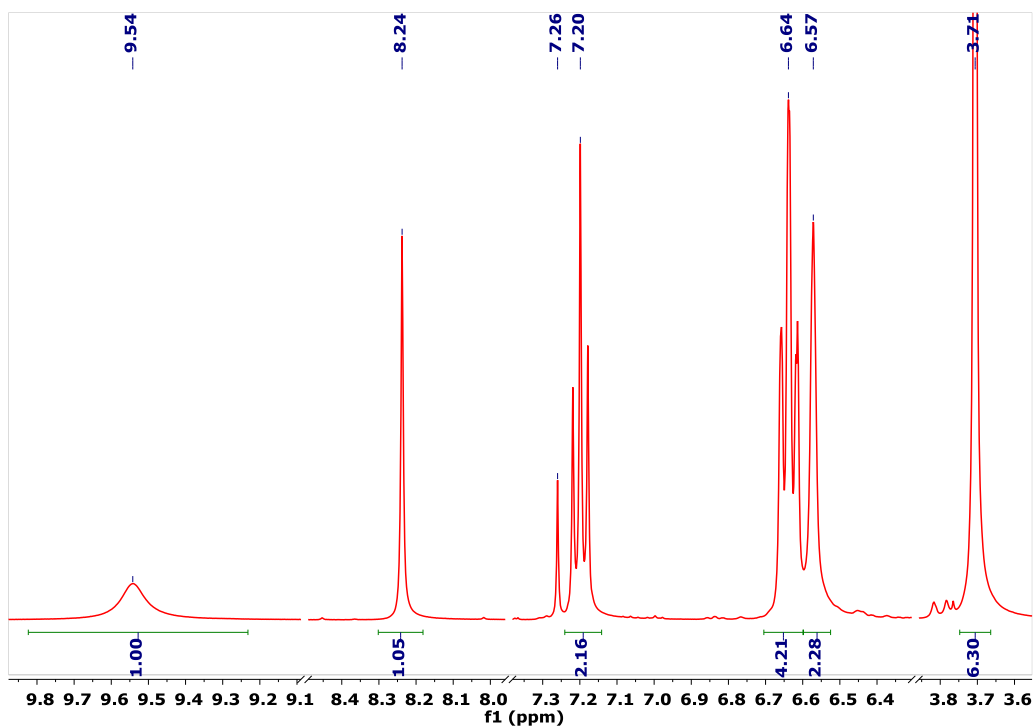


Figure A.2. ¹H NMR spectrum of D^mAniF vs CDCl₃.

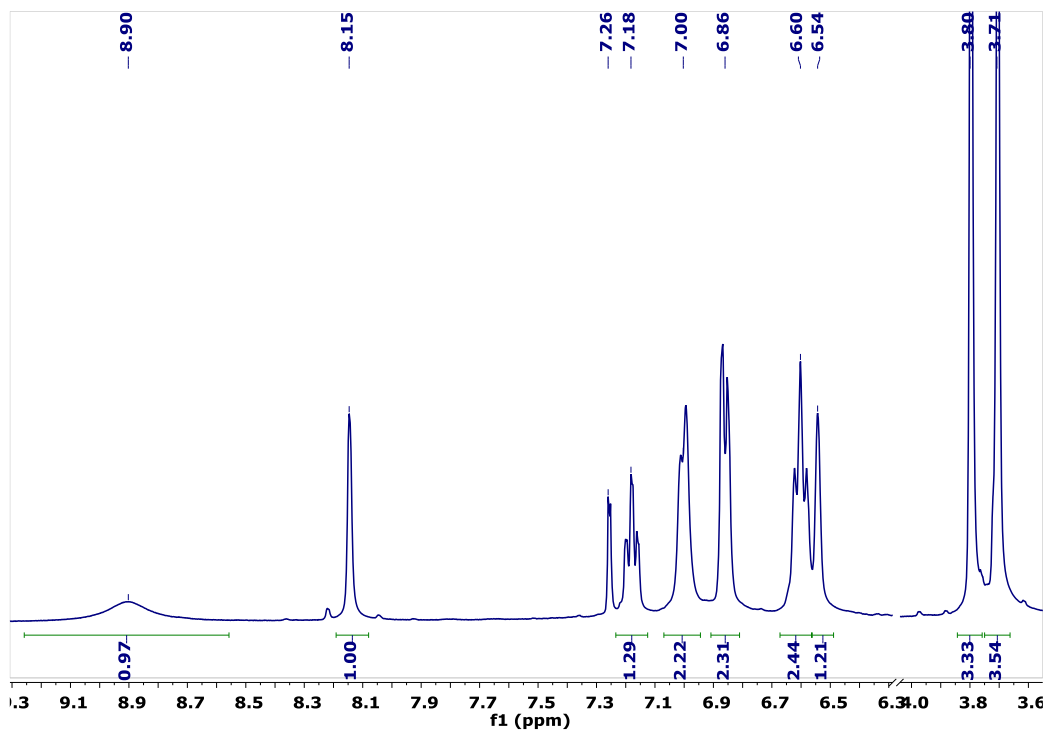


Figure A.3. ^1H NMR spectrum of **1** vs CDCl_3 .

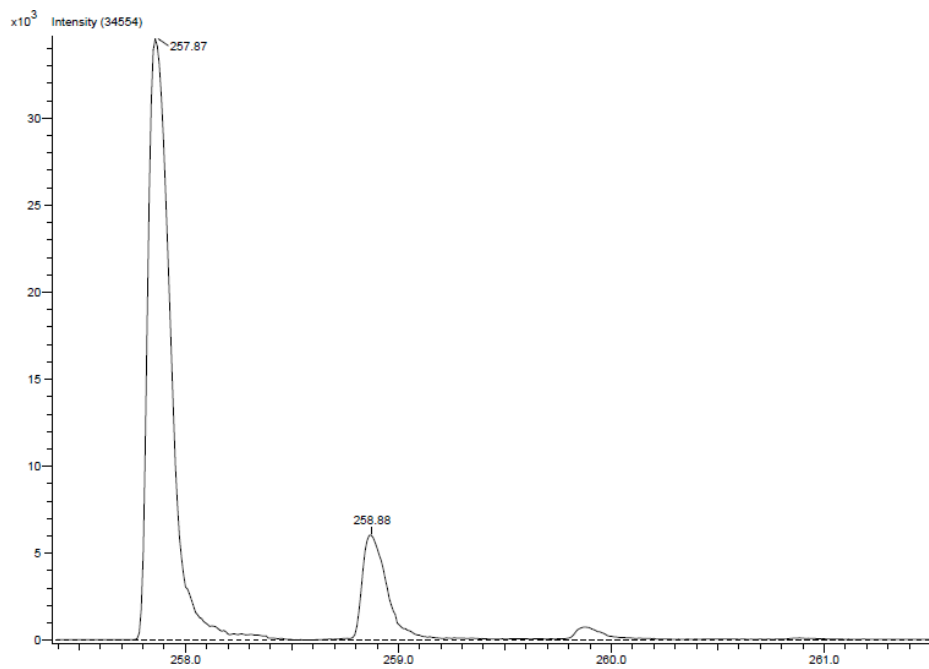


Figure A.4 LCMS of **1**.

Table A.1. Bond lengths (Å) for **1**.

N1-C1	1.3516(19)	N1-C2	1.4110(18)
N1-H1N	0.89(2)	N2-C1	1.2899(19)
N2-C9	1.4134(18)	O1-C4	1.3661(19)
O1-C8	1.4337(19)	O2-C12	1.3713(18)
O2-C15	1.429(2)	C1-H1	0.989(18)
C2-C3	1.391(2)	C2-C7	1.396(2)
C3-C4	1.397(2)	C3-H3	0.95
C4-C5	1.398(2)	C5-C6	1.379(2)
C5-H5	0.95	C6-C7	1.396(2)
C6-H6	0.95	C7-H7	0.95
C8-H8A	0.98	C8-H8B	0.98
C8-H8C	0.98	C9-C10	1.397(2)
C9-C14	1.399(2)	C10-C11	1.392(2)
C10-H10	0.95	C11-C12	1.392(2)
C11-H11	0.95	C12-C13	1.397(2)
C13-C14	1.384(2)	C13-H13	0.95
C14-H14	0.95	C15-H15A	0.98
C15-H15B	0.98	C15-H15C	0.98

Table A.2. Bond angles (°) for **1**.

C1-N1-C2	126.10(13)	C1-N1-H1N	115.9(13)
C2-N1-H1N	117.3(13)	C1-N2-C9	118.11(12)
C4-O1-C8	117.40(12)	C12-O2-C15	117.64(12)
N2-C1-N1	121.00(14)	N2-C1-H1	121.2(10)
N1-C1-H1	117.7(10)	C3-C2-C7	120.74(14)
C3-C2-N1	116.24(13)	C7-C2-N1	123.02(14)
C2-C3-C4	119.98(13)	C2-C3-H3	120.0
C4-C3-H3	120.0	O1-C4-C3	123.78(13)
O1-C4-C5	116.40(13)	C3-C4-C5	119.82(14)
C6-C5-C4	119.27(14)	C6-C5-H5	120.4
C4-C5-H5	120.4	C5-C6-C7	122.00(14)
C5-C6-H6	119.0	C7-C6-H6	119.0
C6-C7-C2	118.17(14)	C6-C7-H7	120.9
C2-C7-H7	120.9	O1-C8-H8A	109.5
O1-C8-H8B	109.5	H8A-C8-H8B	109.5

O1-C8-H8C	109.5	H8A-C8-H8C	109.5
H8B-C8-H8C	109.5	C10-C9-C14	117.83(14)
C10-C9-N2	119.02(13)	C14-C9-N2	123.07(13)
C11-C10-C9	121.75(14)	C11-C10-H10	119.1
C9-C10-H10	119.1	C10-C11-C12	119.55(14)
C10-C11-H11	120.2	C12-C11-H11	120.2
O2-C12-C11	124.37(14)	O2-C12-C13	116.26(13)
C11-C12-C13	119.37(14)	C14-C13-C12	120.55(14)
C14-C13-H13	119.7	C12-C13-H13	119.7
C13-C14-C9	120.94(14)	C13-C14-H14	119.5
C9-C14-H14	119.5	O2-C15-H15A	109.5
O2-C15-H15B	109.5	H15A-C15-H15B	109.5
O2-C15-H15C	109.5	H15A-C15-H15C	109.5
H15B-C15-H15C	109.5		

Table A.3. Torsion angles (°) for **1**.

C9-N2-C1-N1	-179.41(13)	C2-N1-C1-N2	-167.50(14)
C1-N1-C2-C3	154.11(14)	C1-N1-C2-C7	-26.9(2)
C7-C2-C3-C4	0.3(2)	N1-C2-C3-C4	179.35(13)
C8-O1-C4-C3	1.5(2)	C8-O1-C4-C5	-177.96(13)
C2-C3-C4-O1	-178.36(13)	C2-C3-C4-C5	1.1(2)
O1-C4-C5-C6	177.83(13)	C3-C4-C5-C6	-1.7(2)
C4-C5-C6-C7	0.8(2)	C5-C6-C7-C2	0.6(2)
C3-C2-C7-C6	-1.2(2)	N1-C2-C7-C6	179.89(13)
C1-N2-C9-C10	-127.17(15)	C1-N2-C9-C14	56.3(2)
C14-C9-C10-C11	-0.8(2)	N2-C9-C10-C11	-177.58(13)
C9-C10-C11-C12	1.2(2)	C15-O2-C12-C11	-11.2(2)
C15-O2-C12-C13	168.70(14)	C10-C11-C12-O2	178.95(14)
C10-C11-C12-C13	-1.0(2)	O2-C12-C13-C14	-179.50(14)
C11-C12-C13-C14	0.4(2)	C12-C13-C14-C9	-0.1(2)
C10-C9-C14-C13	0.3(2)	N2-C9-C14-C13	176.87(14)

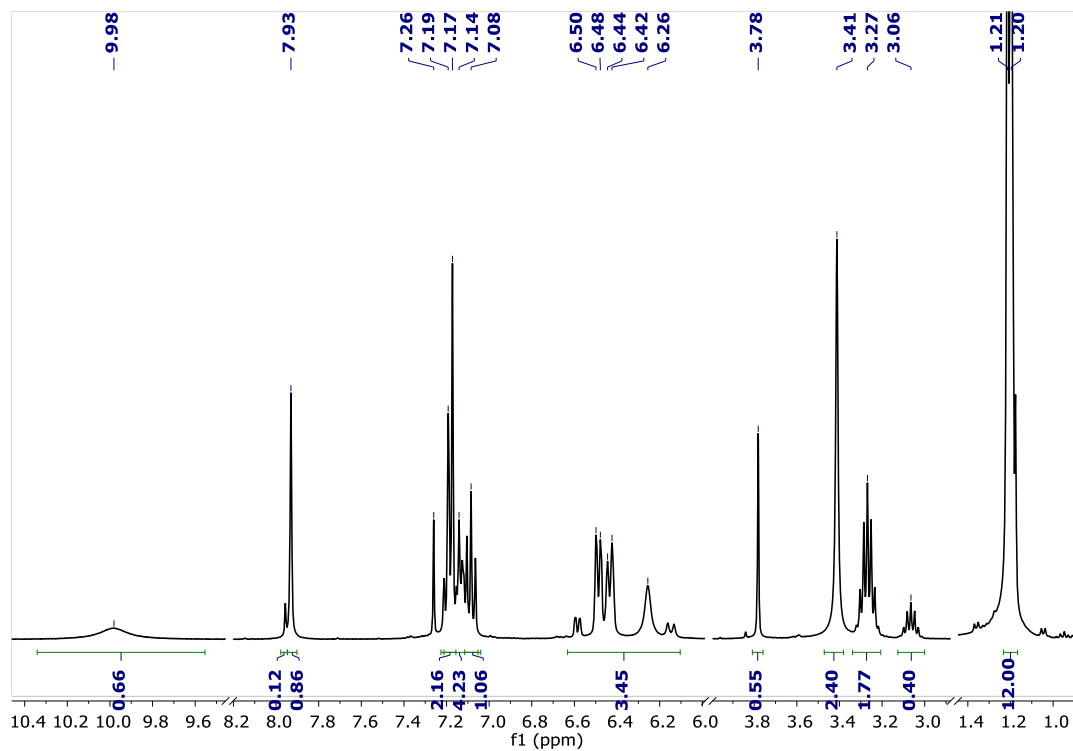


Figure A.5. ^1H NMR spectrum of **2** vs CDCl_3

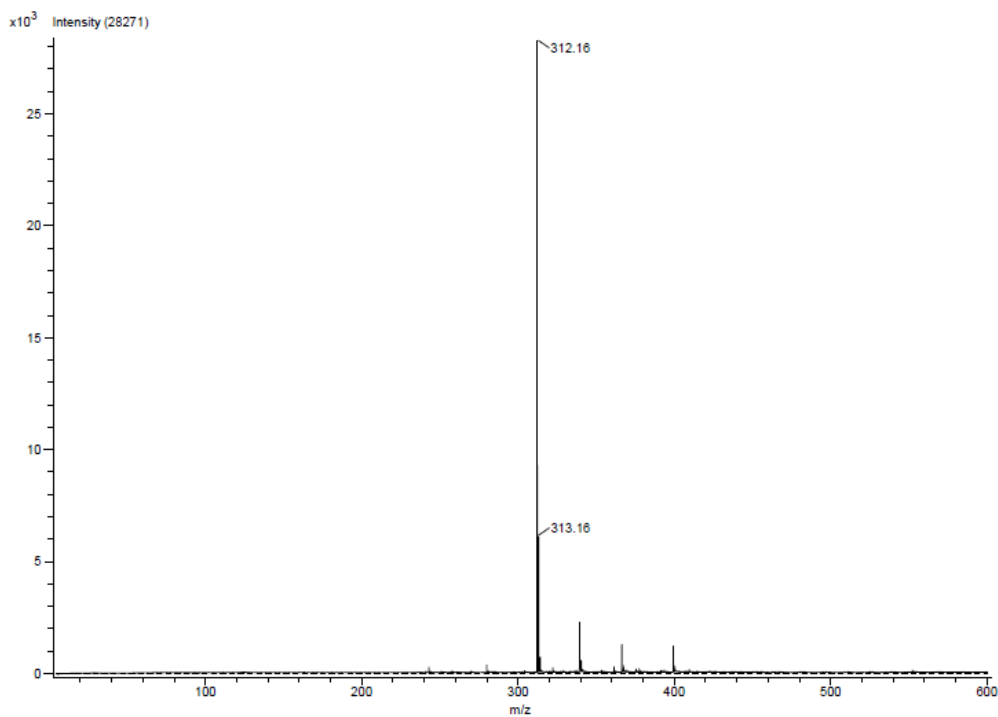


Figure A.6. LCMS of **2**.

Table A.4. Bond lengths (Å) for **2**.

O2-C24	1.379(3)	O2-C28	1.415(3)
N4-C21	1.280(3)	N4-C29	1.433(3)
N1-C1	1.351(3)	N1-C2	1.409(3)
N1-H1N	0.90(2)	N2-C1	1.279(3)
N2-C9	1.434(3)	N3-C21	1.357(3)
N3-C22	1.416(3)	N3-H2N	0.90(3)
O1-C4	1.371(3)	O1-C8	1.429(3)
C29-C34	1.405(3)	C29-C30	1.408(3)
C23-C24	1.393(3)	C23-C22	1.398(3)
C23-H23	0.93	C21-H21	0.93
C22-C27	1.373(3)	C9-C10	1.400(3)
C9-C14	1.412(3)	C3-C4	1.376(3)
C3-C2	1.392(3)	C3-H3	0.93
C1-H1	0.93	C2-C7	1.391(3)
C24-C25	1.375(4)	C30-C31	1.401(3)
C30-C35	1.523(4)	C34-C33	1.398(3)
C34-C38	1.514(4)	C14-C13	1.391(4)
C14-C18	1.524(4)	C4-C5	1.397(4)
C10-C11	1.387(4)	C10-C15	1.517(4)
C35-C36	1.529(4)	C35-C37	1.537(4)
C35-H35	0.98	C13-C12	1.370(4)
C13-H13	0.93	C7-C6	1.376(4)
C7-H7	0.93	C27-C26	1.393(3)
C27-H27	0.93	C18-C20	1.533(4)
C18-C19	1.534(4)	C18-H18	0.98
C25-C26	1.369(4)	C25-H25	0.93
C33-C32	1.378(4)	C33-H33	0.93
C38-C40	1.515(4)	C38-C39	1.529(4)
C38-H38	0.98	C31-C32	1.369(4)
C31-H31	0.93	C5-C6	1.373(4)
C5-H5	0.93	C12-C11	1.369(4)
C12-H12	0.93	C11-H11	0.93
C26-H26	0.93	C6-H6	0.93
C15-C16	1.528(4)	C15-C17	1.539(5)

C15-H15	0.98	C32-H32	0.93
C28-H28A	0.96	C28-H28B	0.96
C28-H28C	0.96	C36-H36A	0.96
C36-H36B	0.96	C36-H36C	0.96
C8-H8A	0.96	C8-H8B	0.96
C8-H8C	0.96	C37-H37A	0.96
C37-H37B	0.96	C37-H37C	0.96
C19-H19A	0.96	C19-H19B	0.96
C19-H19C	0.96	C39-H39A	0.96
C39-H39B	0.96	C39-H39C	0.96
C20-H20A	0.96	C20-H20B	0.96
C20-H20C	0.96	C40-H40A	0.96
C40-H40B	0.96	C40-H40C	0.96
C16-H16A	0.96	C16-H16B	0.96
C16-H16C	0.96	C17-H17A	0.96
C17-H17B	0.96	C17-H17C	0.96

Table A.5. Bond angles (°) for **2**.

C24-O2-C28	117.05(18)	C21-N4-C29	118.21(18)
C1-N1-C2	125.8(2)	C1-N1-H1N	116.9(15)
C2-N1-H1N	116.8(15)	C1-N2-C9	117.84(18)
C21-N3-C22	125.9(2)	C21-N3-H2N	116.8(16)
C22-N3-H2N	117.2(16)	C4-O1-C8	117.1(2)
C34-C29-C30	121.6(2)	C34-C29-N4	118.3(2)
C30-C29-N4	119.9(2)	C24-C23-C22	119.9(2)
C24-C23-H23	120.0	C22-C23-H23	120.0
N4-C21-N3	121.4(2)	N4-C21-H21	119.3
N3-C21-H21	119.3	C27-C22-C23	119.9(2)
C27-C22-N3	123.6(2)	C23-C22-N3	116.5(2)
C10-C9-C14	121.7(2)	C10-C9-N2	120.7(2)
C14-C9-N2	117.5(2)	C4-C3-C2	120.1(2)
C4-C3-H3	119.9	C2-C3-H3	119.9
N2-C1-N1	121.6(2)	N2-C1-H1	119.2
N1-C1-H1	119.2	C7-C2-C3	119.9(2)
C7-C2-N1	122.8(2)	C3-C2-N1	117.3(2)
C25-C24-O2	116.3(2)	C25-C24-C23	120.2(2)
O2-C24-C23	123.4(2)	C31-C30-C29	117.5(2)
C31-C30-C35	121.0(2)	C29-C30-C35	121.5(2)

C33-C34-C29	117.6(2)	C33-C34-C38	122.0(2)
C29-C34-C38	120.4(2)	C13-C14-C9	116.9(2)
C13-C14-C18	121.8(2)	C9-C14-C18	121.2(2)
O1-C4-C3	124.1(2)	O1-C4-C5	116.1(2)
C3-C4-C5	119.8(2)	C11-C10-C9	118.0(3)
C11-C10-C15	120.2(3)	C9-C10-C15	121.8(2)
C30-C35-C36	111.2(2)	C30-C35-C37	113.2(2)
C36-C35-C37	110.4(2)	C30-C35-H35	107.2
C36-C35-H35	107.2	C37-C35-H35	107.2
C12-C13-C14	122.0(3)	C12-C13-H13	119.0
C14-C13-H13	119.0	C6-C7-C2	119.3(3)
C6-C7-H7	120.3	C2-C7-H7	120.3
C22-C27-C26	118.7(2)	C22-C27-H27	120.7
C26-C27-H27	120.7	C14-C18-C20	113.5(3)
C14-C18-C19	110.1(2)	C20-C18-C19	111.0(3)
C14-C18-H18	107.3	C20-C18-H18	107.3
C19-C18-H18	107.3	C26-C25-C24	118.9(2)
C26-C25-H25	120.6	C24-C25-H25	120.6
C32-C33-C34	121.6(3)	C32-C33-H33	119.2
C34-C33-H33	119.2	C34-C38-C40	113.3(3)
C34-C38-C39	111.2(2)	C40-C38-C39	111.0(3)
C34-C38-H38	107.0	C40-C38-H38	107.0
C39-C38-H38	107.0	C32-C31-C30	121.7(3)
C32-C31-H31	119.1	C30-C31-H31	119.1
C6-C5-C4	119.6(2)	C6-C5-H5	120.2
C4-C5-H5	120.2	C11-C12-C13	120.0(3)
C11-C12-H12	120.0	C13-C12-H12	120.0
C12-C11-C10	121.4(3)	C12-C11-H11	119.3
C10-C11-H11	119.3	C25-C26-C27	122.3(3)
C25-C26-H26	118.8	C27-C26-H26	118.8
C5-C6-C7	121.2(2)	C5-C6-H6	119.4
C7-C6-H6	119.4	C10-C15-C16	111.1(3)
C10-C15-C17	113.6(3)	C16-C15-C17	111.1(3)
C10-C15-H15	106.9	C16-C15-H15	106.9
C17-C15-H15	106.9	C31-C32-C33	119.9(3)
C31-C32-H32	120.1	C33-C32-H32	120.1
O2-C28-H28A	109.5	O2-C28-H28B	109.5

H28A-C28-H28B	109.5	O2-C28-H28C	109.5
H28A-C28-H28C	109.5	H28B-C28-H28C	109.5
C35-C36-H36A	109.5	C35-C36-H36B	109.5
H36A-C36-H36B	109.5	C35-C36-H36C	109.5
H36A-C36-H36C	109.5	H36B-C36-H36C	109.5
O1-C8-H8A	109.5	O1-C8-H8B	109.5
H8A-C8-H8B	109.5	O1-C8-H8C	109.5
H8A-C8-H8C	109.5	H8B-C8-H8C	109.5
C35-C37-H37A	109.5	C35-C37-H37B	109.5
H37A-C37-H37B	109.5	C35-C37-H37C	109.5
H37A-C37-H37C	109.5	H37B-C37-H37C	109.5
C18-C19-H19A	109.5	C18-C19-H19B	109.5
H19A-C19-H19B	109.5	C18-C19-H19C	109.5
H19A-C19-H19C	109.5	H19B-C19-H19C	109.5
C38-C39-H39A	109.5	C38-C39-H39B	109.5
H39A-C39-H39B	109.5	C38-C39-H39C	109.5
H39A-C39-H39C	109.5	H39B-C39-H39C	109.5
C18-C20-H20A	109.5	C18-C20-H20B	109.5
H20A-C20-H20B	109.5	C18-C20-H20C	109.5
H20A-C20-H20C	109.5	H20B-C20-H20C	109.5
C38-C40-H40A	109.5	C38-C40-H40B	109.5
H40A-C40-H40B	109.5	C38-C40-H40C	109.5
H40A-C40-H40C	109.5	H40B-C40-H40C	109.5
C15-C16-H16A	109.5	C15-C16-H16B	109.5
H16A-C16-H16B	109.5	C15-C16-H16C	109.5
H16A-C16-H16C	109.5	H16B-C16-H16C	109.5

C15-C17-H17A	109.5	C15-C17-H17B	109.5
H17A-C17-H17B	109.5	C15-C17-H17C	109.5
H17A-C17-H17C	109.5	H17B-C17-H17C	109.5

Table A.6. Torsion angles (°) for **2**.

C21-N4-C29-C34	98.3(2)	C21-N4-C29-C30	-87.1(3)
C29-N4-C21-N3	-174.7(2)	C22-N3-C21-N4	-169.4(2)
C24-C23-C22-C27	0.9(4)	C24-C23-C22-N3	-177.0(2)
C21-N3-C22-C27	12.2(4)	C21-N3-C22-C23	-170.0(2)
C1-N2-C9-C10	85.9(3)	C1-N2-C9-C14	-97.6(2)
C9-N2-C1-N1	174.8(2)	C2-N1-C1-N2	174.1(2)
C4-C3-C2-C7	1.5(4)	C4-C3-C2-N1	179.0(2)
C1-N1-C2-C7	-19.7(4)	C1-N1-C2-C3	162.8(2)
C28-O2-C24-C25	-178.1(3)	C28-O2-C24-C23	2.0(4)
C22-C23-C24-C25	-1.8(4)	C22-C23-C24-O2	178.0(2)
C34-C29-C30-C31	-2.8(3)	N4-C29-C30-C31	-177.2(2)
C34-C29-C30-C35	178.2(2)	N4-C29-C30-C35	3.8(3)
C30-C29-C34-C33	3.9(3)	N4-C29-C34-C33	178.4(2)
C30-C29-C34-C38	-177.9(2)	N4-C29-C34-C38	-3.4(3)
C10-C9-C14-C13	-3.9(3)	N2-C9-C14-C13	179.6(2)
C10-C9-C14-C18	178.2(2)	N2-C9-C14-C18	1.6(3)
C8-O1-C4-C3	10.3(4)	C8-O1-C4-C5	-169.3(3)
C2-C3-C4-O1	-180.0(2)	C2-C3-C4-C5	-0.4(4)
C14-C9-C10-C11	3.4(3)	N2-C9-C10-C11	179.9(2)
C14-C9-C10-C15	-177.9(2)	N2-C9-C10-C15	-1.4(4)
C31-C30-C35-C36	-83.3(3)	C29-C30-C35-C36	95.8(3)
C31-C30-C35-C37	41.7(3)	C29-C30-C35-C37	-139.2(3)
C9-C14-C13-C12	1.3(4)	C18-C14-C13-C12	179.2(2)

C3-C2-C7-C6	-2.0(4)	N1-C2-C7-C6	-179.4(3)
C23-C22-C27-C26	0.6(4)	N3-C22-C27-C26	178.4(3)
C13-C14-C18-C20	43.7(3)	C9-C14-C18-C20	-138.4(3)
C13-C14-C18-C19	-81.4(3)	C9-C14-C18-C19	96.4(3)
O2-C24-C25-C26	-178.7(3)	C23-C24-C25-C26	1.2(4)
C29-C34-C33-C32	-2.6(4)	C38-C34-C33-C32	179.2(3)
C33-C34-C38-C40	-42.5(4)	C29-C34-C38-C40	139.3(3)
C33-C34-C38-C39	83.4(3)	C29-C34-C38-C39	-94.8(3)
C29-C30-C31-C32	0.3(4)	C35-C30-C31-C32	179.4(3)
O1-C4-C5-C6	179.4(3)	C3-C4-C5-C6	-0.2(4)
C14-C13-C12-C11	1.8(4)	C13-C12-C11-C10	-2.3(4)
C9-C10-C11-C12	-0.3(4)	C15-C10-C11-C12	-179.0(3)
C24-C25-C26-C27	0.4(5)	C22-C27-C26-C25	-1.3(5)
C4-C5-C6-C7	-0.3(5)	C2-C7-C6-C5	1.4(5)
C11-C10-C15-C16	77.8(3)	C9-C10-C15-C16	-100.8(3)
C11-C10-C15-C17	-48.3(4)	C9-C10-C15-C17	133.0(3)
C30-C31-C32-C33	1.0(4)	C34-C33-C32-C31	0.3(4)

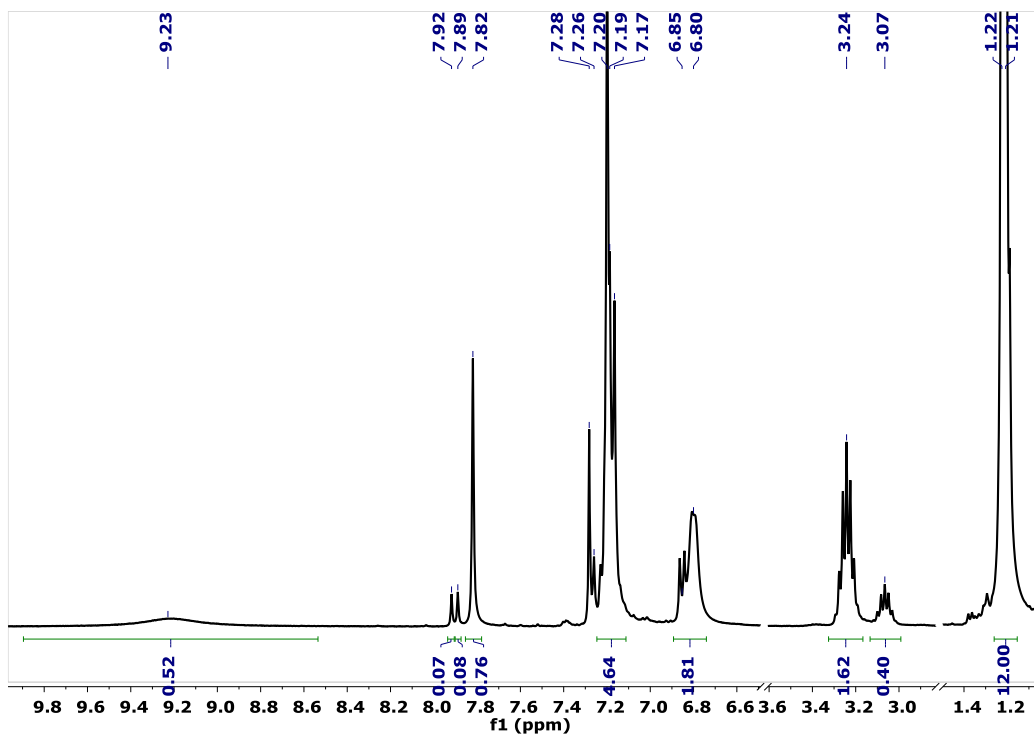


Figure A.7. ^1H NMR spectrum of **3** vs CDCl_3 .

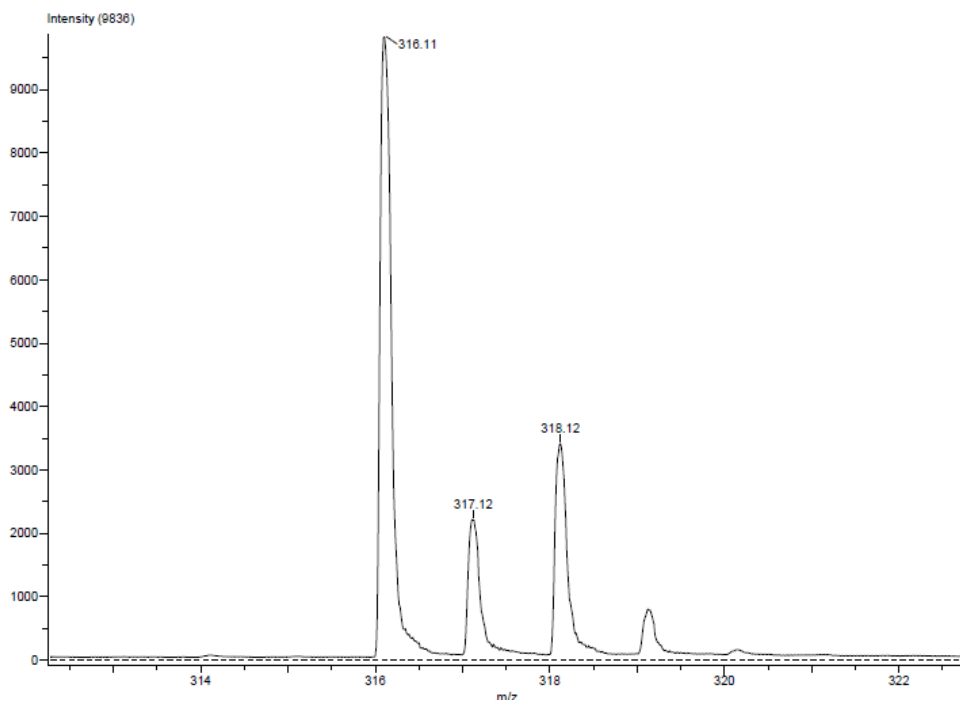


Figure A.8. LCMS of **3**.

Table A.7. Bond lengths (\AA) for **3**.

C11-C1	1.749(3)	N1-C7	1.292(3)
N1-C4	1.413(3)	N2-C7	1.338(3)
N2-C8	1.440(3)	N2-H2N	0.81(3)
C1-C2	1.368(4)	C1-C6	1.374(4)
C2-C3	1.381(4)	C2-H2	0.95
C3-C4	1.383(4)	C3-H3	0.95
C4-C5	1.386(4)	C5-C6	1.386(4)
C5-H5	0.95	C6-H6	0.95
C7-H7	0.95	C8-C13	1.405(4)
C8-C9	1.407(4)	C9-C10	1.382(4)
C9-C14	1.520(4)	C10-C11	1.382(4)
C10-H10	0.95	C11-C12	1.379(4)
C11-H11	0.95	C12-C13	1.396(4)
C12-H12	0.95	C13-C17	1.518(4)
C14-C15	1.509(4)	C14-C16	1.511(4)
C14-H14	1.0	C15-H15A	0.98
C15-H15B	0.98	C15-H15C	0.98
C16-H16A	0.98	C16-H16B	0.98
C16-H16C	0.98	C17-C19	1.506(4)
C17-C18	1.510(5)	C17-H17	1.0
C18-H18A	0.98	C18-H18B	0.98
C18-H18C	0.98	C19-H19A	0.98
C19-H19B	0.98	C19-H19C	0.98

Table A.8. Bond angles (°) for **3**.

C7-N1-C4	116.0(2)	C7-N2-C8	125.6(2)
C7-N2-H2N	118.(2)	C8-N2-H2N	117.(2)
C2-C1-C6	120.9(3)	C2-C1-C11	120.0(3)
C6-C1-C11	119.1(3)	C1-C2-C3	119.3(3)
C1-C2-H2	120.3	C3-C2-H2	120.3
C2-C3-C4	121.6(3)	C2-C3-H3	119.2
C4-C3-H3	119.2	C3-C4-C5	117.7(3)
C3-C4-N1	119.7(3)	C5-C4-N1	122.5(3)
C6-C5-C4	121.3(3)	C6-C5-H5	119.3
C4-C5-H5	119.3	C1-C6-C5	119.1(3)
C1-C6-H6	120.4	C5-C6-H6	120.4
N1-C7-N2	124.3(3)	N1-C7-H7	117.9
N2-C7-H7	117.9	C13-C8-C9	121.9(2)

C13-C8-N2	119.0(2)	C9-C8-N2	118.9(2)
C10-C9-C8	117.9(3)	C10-C9-C14	121.8(3)
C8-C9-C14	120.3(2)	C9-C10-C11	121.4(3)
C9-C10-H10	119.3	C11-C10-H10	119.3
C12-C11-C10	120.0(3)	C12-C11-H11	120.0
C10-C11-H11	120.0	C11-C12-C13	121.5(3)
C11-C12-H12	119.3	C13-C12-H12	119.3
C12-C13-C8	117.3(3)	C12-C13-C17	120.1(3)
C8-C13-C17	122.6(2)	C15-C14-C16	111.4(3)
C15-C14-C9	113.8(2)	C16-C14-C9	110.1(2)
C15-C14-H14	107.1	C16-C14-H14	107.1
C9-C14-H14	107.1	C14-C15-H15A	109.5
C14-C15-H15B	109.5	H15A-C15-H15B	109.5
C14-C15-H15C	109.5	H15A-C15-H15C	109.5
H15B-C15-H15C	109.5	C14-C16-H16A	109.5
C14-C16-H16B	109.5	H16A-C16-H16B	109.5
C14-C16-H16C	109.5	H16A-C16-H16C	109.5
H16B-C16-H16C	109.5	C19-C17-C18	109.7(3)
C19-C17-C13	112.4(2)	C18-C17-C13	111.6(3)
C19-C17-H17	107.6	C18-C17-H17	107.6
C13-C17-H17	107.6	C17-C18-H18A	109.5
C17-C18-H18B	109.5	H18A-C18-H18B	109.5
C17-C18-H18C	109.5	H18A-C18-H18C	109.5
H18B-C18-H18C	109.5	C17-C19-H19A	109.5
C17-C19-H19B	109.5	H19A-C19-H19B	109.5
C17-C19-H19C	109.5	H19A-C19-H19C	109.5
H19B-C19-H19C	109.5		

Table A.9. Torsion angles (°) for **3**.

C6-C1-C2-C3	-0.7(5)	C11-C1-C2-C3	178.5(2)
C1-C2-C3-C4	0.2(4)	C2-C3-C4-C5	-0.3(4)
C2-C3-C4-N1	-176.8(3)	C7-N1-C4-C3	-124.5(3)
C7-N1-C4-C5	59.1(3)	C3-C4-C5-C6	0.8(4)
N1-C4-C5-C6	177.2(2)	C2-C1-C6-C5	1.2(5)
C11-C1-C6-C5	-178.0(2)	C4-C5-C6-C1	-1.3(4)
C4-N1-C7-N2	-174.4(3)	C8-N2-C7-N1	7.5(4)
C7-N2-C8-C13	74.2(3)	C7-N2-C8-C9	-110.0(3)
C13-C8-C9-C10	1.2(4)	N2-C8-C9-C10	-174.5(2)

C13-C8-C9-C14	-178.2(2)	N2-C8-C9-C14	6.1(4)
C8-C9-C10-C11	-0.9(4)	C14-C9-C10-C11	178.5(2)
C9-C10-C11-C12	-0.3(4)	C10-C11-C12-C13	1.3(4)
C11-C12-C13-C8	-1.0(4)	C11-C12-C13-C17	176.9(3)
C9-C8-C13-C12	-0.3(4)	N2-C8-C13-C12	175.4(2)
C9-C8-C13-C17	-178.2(2)	N2-C8-C13-C17	-2.5(4)
C10-C9-C14-C15	27.3(4)	C8-C9-C14-C15	-153.3(3)
C10-C9-C14-C16	-98.5(3)	C8-C9-C14-C16	80.8(3)
C12-C13-C17-C19	53.8(4)	C8-C13-C17-C19	-128.4(3)
C12-C13-C17-C18	-70.0(4)	C8-C13-C17-C18	107.9(3)

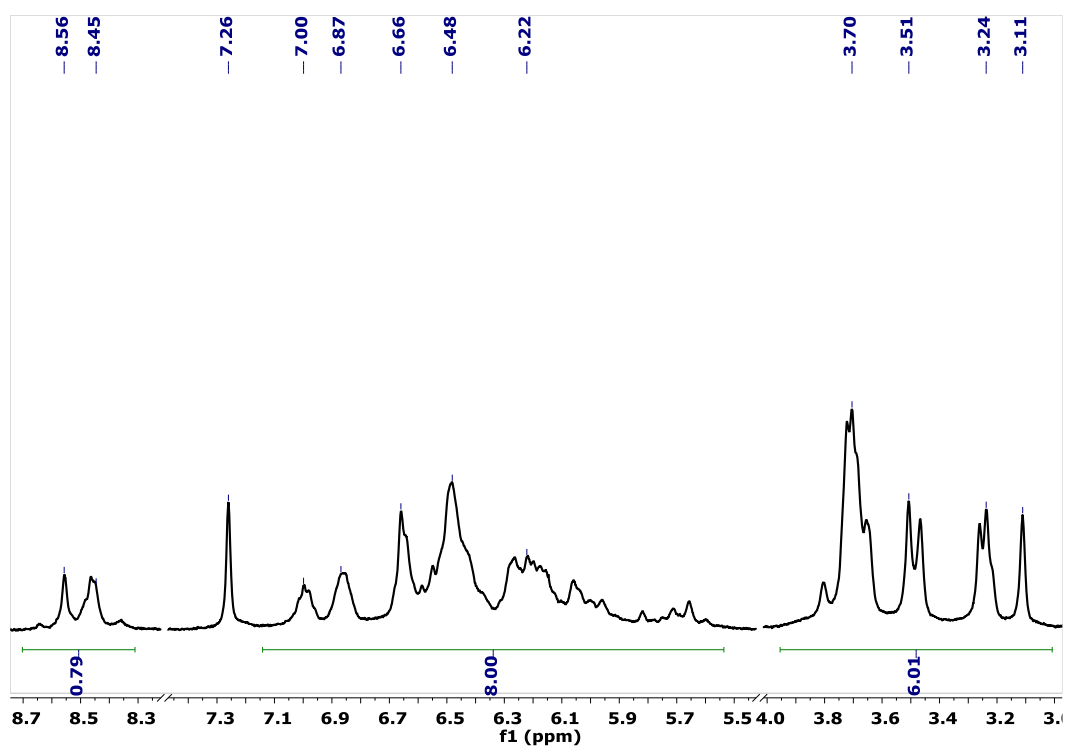


Figure A.9. ^1H NMR spectrum of **5** vs CDCl_3 .

Table A.10. Bond lengths (\AA) for **5**.

Mo1-Mo1	2.0991(9)	Mo1-N1	2.154(3)
Mo1-N1	2.154(3)	Mo1-N2	2.169(3)
Mo1-N2	2.169(3)	O1-C4	1.366(6)
O1-C8	1.429(7)	O2-C12	1.369(6)
O2-C15	1.429(8)	N1-C1	1.327(5)

N1-C2	1.414(5)	N2-C1	1.322(5)
N2-C9	1.433(5)	C1-H1	0.95
C2-C7	1.392(6)	C2-C3	1.409(6)
C3-C4	1.392(6)	C3-H3	0.95
C4-C5	1.387(7)	C5-C6	1.381(7)
C5-H5	0.95	C6-C7	1.393(7)
C6-H6	0.95	C7-H7	0.95
C8-H8A	0.98	C8-H8B	0.98
C8-H8C	0.98	C9-C14	1.387(6)
C9-C10	1.388(6)	C10-C11	1.398(7)
C10-H10	0.95	C11-C12	1.381(8)
C11-H11	0.95	C12-C13	1.383(8)
C13-C14	1.404(7)	C13-H13	0.95
C14-H14	0.95	C15-H15A	0.98
C15-H15B	0.98	C15-H15C	0.98

Table A.11. Bond angles (°) for **5**.

Mo1-Mo1-N1	93.21(9)	Mo1-Mo1-N1	93.21(9)
N1-Mo1-N1	173.57(18)	Mo1-Mo1-N2	92.17(9)
N1-Mo1-N2	89.49(13)	N1-Mo1-N2	90.26(13)
Mo1-Mo1-N2	92.17(9)	N1-Mo1-N2	90.26(13)
N1-Mo1-N2	89.49(13)	N2-Mo1-N2	175.65(18)
C4-O1-C8	116.8(4)	C12-O2-C15	117.7(5)
C1-N1-C2	119.8(3)	C1-N1-Mo1	116.7(3)
C2-N1-Mo1	122.4(3)	C1-N2-C9	115.7(3)
C1-N2-Mo1	117.0(3)	C9-N2-Mo1	126.6(3)
N2-C1-N1	120.7(4)	N2-C1-H1	119.6
N1-C1-H1	119.6	C7-C2-C3	118.8(4)
C7-C2-N1	123.3(4)	C3-C2-N1	117.7(4)

C4-C3-C2	120.3(4)	C4-C3-H3	119.8
C2-C3-H3	119.8	O1-C4-C5	115.6(4)
O1-C4-C3	124.1(4)	C5-C4-C3	120.3(4)
C6-C5-C4	119.3(4)	C6-C5-H5	120.3
C4-C5-H5	120.3	C5-C6-C7	121.3(4)
C5-C6-H6	119.4	C7-C6-H6	119.4
C2-C7-C6	119.9(4)	C2-C7-H7	120.0
C6-C7-H7	120.0	O1-C8-H8A	109.5
O1-C8-H8B	109.5	H8A-C8-H8B	109.5
O1-C8-H8C	109.5	H8A-C8-H8C	109.5
H8B-C8-H8C	109.5	C14-C9-C10	118.4(4)
C14-C9-N2	122.1(4)	C10-C9-N2	119.5(4)
C9-C10-C11	120.8(5)	C9-C10-H10	119.6
C11-C10-H10	119.6	C12-C11-C10	120.2(5)
C12-C11-H11	119.9	C10-C11-H11	119.9
O2-C12-C11	115.5(5)	O2-C12-C13	124.6(5)
C11-C12-C13	119.9(5)	C12-C13-C14	119.5(5)
C12-C13-H13	120.2	C14-C13-H13	120.2
C9-C14-C13	121.1(4)	C9-C14-H14	119.4
C13-C14-H14	119.4	O2-C15-H15A	109.5
O2-C15-H15B	109.5	H15A-C15-H15B	109.5
O2-C15-H15C	109.5	H15A-C15-H15C	109.5
H15B-C15-H15C	109.5		

Table A.12. Torsion angles (°) for **5**.

C9-N2-C1-N1	-176.7(4)	Mo1-N2-C1-N1	-5.6(5)
C2-N1-C1-N2	173.2(4)	Mo1-N1-C1-N2	5.2(5)
C1-N1-C2-C7	-28.6(6)	Mo1-N1-C2-C7	138.6(4)
C1-N1-C2-C3	157.3(4)	Mo1-N1-C2-C3	-35.4(5)
C7-C2-C3-C4	-1.6(6)	N1-C2-C3-C4	172.8(4)
C8-O1-C4-C5	170.5(5)	C8-O1-C4-C3	-10.2(7)
C2-C3-C4-O1	-177.7(4)	C2-C3-C4-C5	1.7(7)

O1-C4-C5-C6	179.0(4)	C3-C4-C5-C6	-0.4(7)
C4-C5-C6-C7	-0.9(8)	C3-C2-C7-C6	0.2(7)
N1-C2-C7-C6	-173.8(4)	C5-C6-C7-C2	1.0(7)
C1-N2-C9-C14	-120.3(5)	Mo1-N2-C9-C14	69.6(5)
C1-N2-C9-C10	60.1(5)	Mo1-N2-C9-C10	-110.0(4)
C14-C9-C10-C11	0.2(8)	N2-C9-C10-C11	179.8(5)
C9-C10-C11-C12	0.2(9)	C15-O2-C12-C11	-176.0(6)
C15-O2-C12-C13	3.7(9)	C10-C11-C12-O2	179.9(6)
C10-C11-C12-C13	0.2(9)	O2-C12-C13-C14	179.3(5)
C11-C12-C13-C14	-1.0(9)	C10-C9-C14-C13	-1.0(7)
N2-C9-C14-C13	179.4(4)	C12-C13-C14-C9	1.4(8)

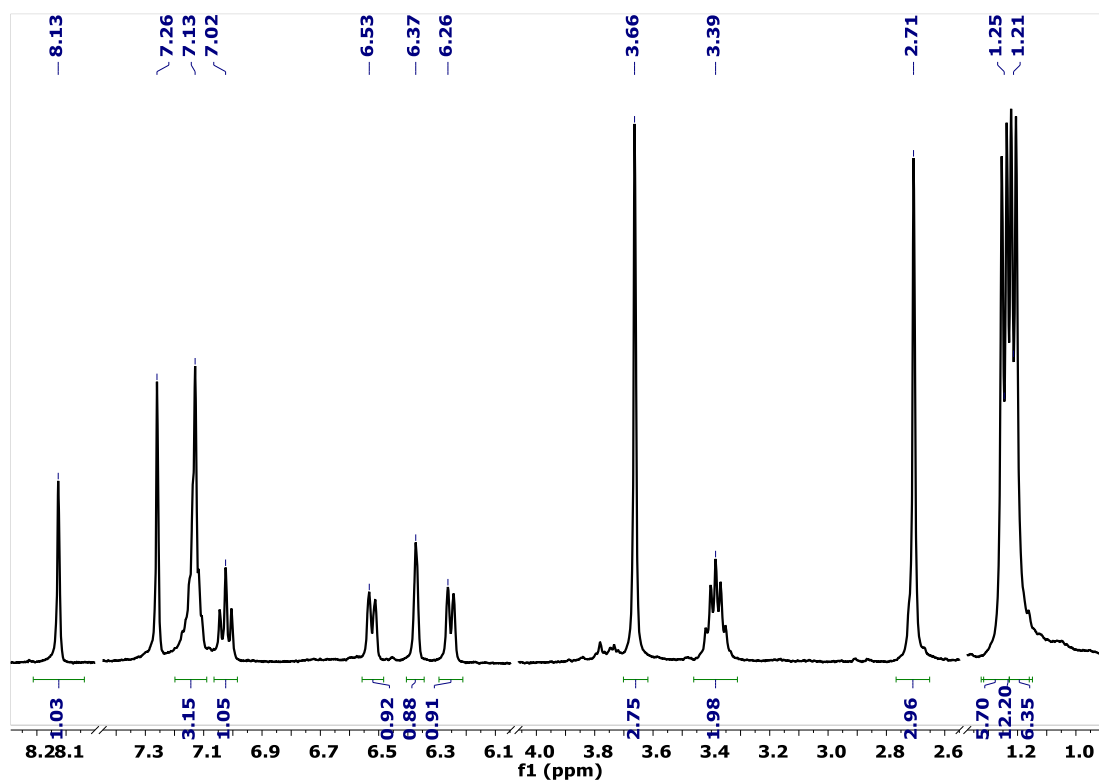


Figure A.10. ^1H NMR spectrum of **6** vs CDCl_3 .

Table A.13. Bond lengths (\AA) for **6**.

Mo01-Mo01	2.1009(2)	Mo01-O1	2.1171(10)
Mo01-O2	2.1255(10)	Mo01-N1	2.1422(12)
Mo01-N2	2.1643(12)	N1-C1	1.3252(19)
N1-C2	1.4270(18)	N2-C1	1.3264(18)
N2-C9	1.4472(18)	N2-Mo01	2.1642(12)
O1-C21	1.272(2)	O2-C21	1.2699(19)

O2-Mo01	2.1255(10)	O3-C4	1.3714(18)
O3-C8	1.432(2)	C2-C7	1.394(2)
C2-C3	1.402(2)	C3-C4	1.395(2)
C4-C5	1.393(2)	C5-C6	1.382(2)
C6-C7	1.392(2)	C9-C14	1.406(2)
C9-C10	1.409(2)	C10-C11	1.398(2)
C10-C15	1.512(2)	C11-C12	1.377(3)
C12-C13	1.383(3)	C13-C14	1.398(2)
C14-C18	1.526(2)	C15-C16	1.519(3)
C15-C17	1.527(3)	C18-C20	1.529(3)
C18-C19	1.530(3)	C21-C22	1.505(2)

Table A.14. Bond angles (°) for **6**.

Mo01-Mo01-O1	92.59(3)	Mo01-Mo01-O2	90.87(3)
O1-Mo01-O2	176.07(4)	Mo01-Mo01-N1	92.86(3)
O1-Mo01-N1	88.50(4)	O2-Mo01-N1	89.46(4)
Mo01-Mo01-N2	92.66(3)	O1-Mo01-N2	90.09(4)
O2-Mo01-N2	91.62(4)	N1-Mo01-N2	174.36(4)
C1-N1-C2	115.52(12)	C1-N1-Mo01	117.15(9)
C2-N1-Mo01	127.15(9)	C1-N2-C9	113.77(12)
C1-N2-Mo01	116.22(9)	C9-N2-Mo01	129.84(9)
C21-O1-Mo01	116.30(9)	C21-O2-Mo01	117.52(10)
C4-O3-C8	117.00(13)	N1-C1-N2	121.07(13)
C7-C2-C3	120.45(13)	C7-C2-N1	120.67(13)
C3-C2-N1	118.87(13)	C4-C3-C2	119.00(14)
O3-C4-C5	115.05(14)	O3-C4-C3	124.43(15)
C5-C4-C3	120.52(14)	C6-C5-C4	119.85(15)
C5-C6-C7	120.67(15)	C6-C7-C2	119.49(14)
C14-C9-C10	121.05(14)	C14-C9-N2	119.49(13)
C10-C9-N2	119.45(13)	C11-C10-C9	118.27(15)
C11-C10-C15	120.72(15)	C9-C10-C15	120.97(14)
C12-C11-C10	121.23(17)	C11-C12-C13	119.99(16)
C12-C13-C14	121.26(17)	C13-C14-C9	118.20(15)
C13-C14-C18	119.32(15)	C9-C14-C18	122.49(14)
C10-C15-C16	110.40(18)	C10-C15-C17	113.10(18)
C16-C15-C17	110.51(19)	C14-C18-C20	111.83(15)
C14-C18-C19	111.72(15)	C20-C18-C19	110.37(15)
O2-C21-O1	122.66(14)	O2-C21-C22	118.53(15)

O1-C21-C22 118.80(15)

Table A.15. Torsion angles (°) for **6**.

C2-N1-C1-N2	177.53(12)	Mo01-N1-C1-N2	2.02(18)
C9-N2-C1-N1	-176.67(12)	Mo01-N2-C1-N1	-0.83(18)
C1-N1-C2-C7	-50.04(19)	Mo01-N1-C2-C7	124.94(13)
C1-N1-C2-C3	130.74(14)	Mo01-N1-C2-C3	-54.28(17)
C7-C2-C3-C4	0.2(2)	N1-C2-C3-C4	179.38(13)
C8-O3-C4-C5	171.62(16)	C8-O3-C4-C3	-8.4(2)
C2-C3-C4-O3	-179.46(14)	C2-C3-C4-C5	0.5(2)
O3-C4-C5-C6	179.71(16)	C3-C4-C5-C6	-0.2(3)
C4-C5-C6-C7	-0.7(3)	C5-C6-C7-C2	1.3(3)
C3-C2-C7-C6	-1.0(2)	N1-C2-C7-C6	179.75(14)
C1-N2-C9-C14	79.94(17)	Mo01-N2-C9-C14	-95.20(15)
C1-N2-C9-C10	-99.74(16)	Mo01-N2-C9-C10	85.12(16)
C14-C9-C10-C11	-0.1(2)	N2-C9-C10-C11	179.55(15)
C14-C9-C10-C15	-177.63(15)	N2-C9-C10-C15	2.0(2)
C9-C10-C11-C12	-0.1(3)	C15-C10-C11-C12	177.42(19)
C10-C11-C12-C13	0.1(3)	C11-C12-C13-C14	0.0(3)
C12-C13-C14-C9	-0.3(3)	C12-C13-C14-C18	179.17(18)
C10-C9-C14-C13	0.3(2)	N2-C9-C14-C13	-179.38(15)
C10-C9-C14-C18	-179.11(15)	N2-C9-C14-C18	1.2(2)
C11-C10-C15-C16	-85.5(2)	C9-C10-C15-C16	92.0(2)
C11-C10-C15-C17	38.9(3)	C9-C10-C15-C17	-143.63(18)
C13-C14-C18-C20	-53.8(2)	C9-C14-C18-C20	125.57(18)
C13-C14-C18-C19	70.4(2)	C9-C14-C18-C19	-110.16(18)
Mo01-O2-C21-O1	-1.6(2)	Mo01-O2-C21-C22	178.94(13)
Mo01-O1-C21-O2	-0.4(2)	Mo01-O1-C21-C22	179.07(13)

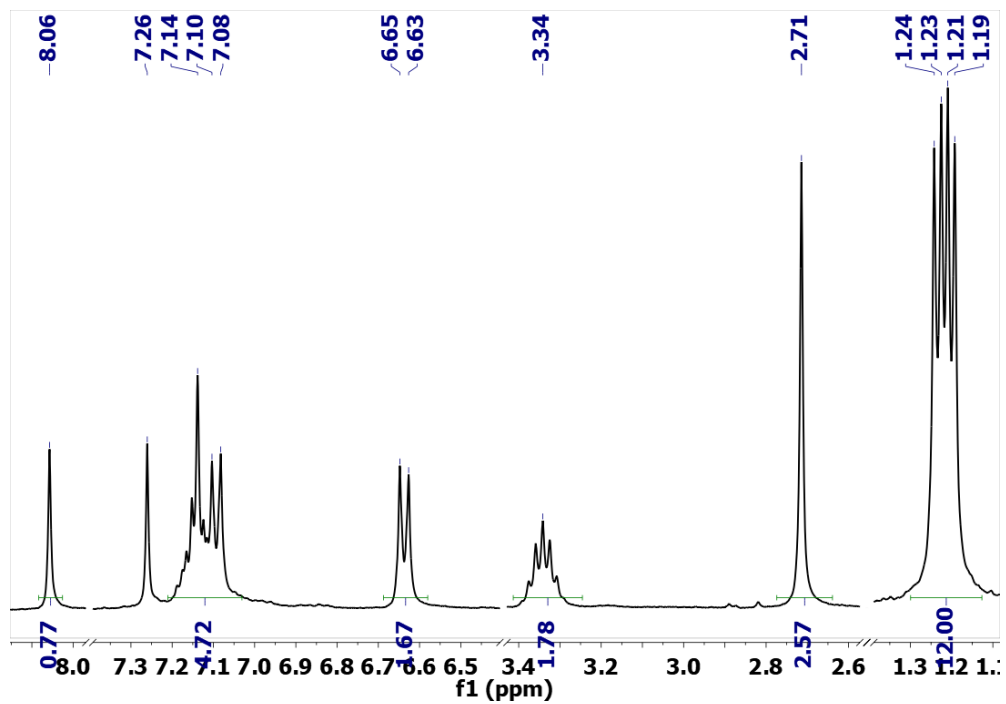


Figure A.11. ^1H NMR spectrum of 7 vs CDCl_3 .

Vita

Iván Alonso Cervantes Martínez was born and raised in Juárez, Chihuahua, México. He attended the University of Texas at El Paso (UTEP) starting on 2013 to pursue a bachelor's degree in chemistry and graduated in 2017. During this time, Iván volunteered two years in the Villagrán laboratory, and another two years he participated as an intern in the annual program MERITUS (Mentored Experiences in Research, Inquiry, and Creativity for Undergraduate Students). He also formed part of the solar outreach program of CCI (Center for Chemical Innovation) from 2015 until the end of the program in 2018. In Fall 2017, Iván continued his studies at UTEP to pursue his Master of Science in Chemistry.

Contact Information: iacervantesmtz4@gmail.com

This thesis was typed by Iván Alonso Cervantes Martínez.